MEASUREMENT OF THE MAGNETIC FIELD OF AN RF-ENCODING BIRDCAGE-COIL DESIGN FOR MAGNETIC RESONANCE IMAGING

A Thesis Submitted to the College of

Graduate Studies and Research

In Partial Fulfillment of the Requirements

For the Degree of Master of Science

In the Division of Biomedical Engineering

University of Saskatchewan

Saskatoon

By

SU WANG

PERMISSION TO USE

In presenting this thesis in partial fulfilment of the requirements for a Postgraduate degree from the University of Saskatchewan, I agree that the Libraries of this University may make it freely available for inspection. I further agree that permission for copying of this thesis in any manner, in whole or in part, for scholarly purposes may be granted by the prof. Gordon Sarty and prof. Michael Bradley who supervised my thesis work or, in their absence, by the Head of the Department or the Dean of the College in which my thesis work was done. It is understood that any copying or publication or use of this thesis or parts thereof for financial gain shall not be allowed without my written permission. It is also understood that due recognition shall be given to me and to the University of Saskatchewan in any scholarly use which may be made of any material in my thesis.

Requests for permission to copy or to make other use of material in this thesis in whole or part should be addressed to:

Head of the Division of Biomedical Engineering

57 Campus Drive

University of Saskatchewan

Saskatoon, Saskatchewan S7N 5A9

Canada

ABSTRACT

Magnetic Resonance Imaging (MRI) is a non-invasive imaging technique used in radiology to investigate the anatomy and physiology of the body in both health and disease. MRI currently depends on the use of magnetic field gradient coils to visualize tissue. However, there is an alternate method, which can only use RF to encode the image. The idea behind RF encoding is that it uses spatial phase variation in the RF transmission to encode spatial information in the MRI signal instead of using gradient magnetic fields. This alternate method of encoding with RF, without magnetic field gradients, allows for a much simpler hardware configuration for the MRI device. Therefore, it could become possible to design a cheaper and lighter portable MRI.

In this study, a measurement device was designed and constructed for a DC model of an RF encoding birdcage coil design. When the appropriate currents were applied onto the legs of the coil, a magnetic field was generated as quantified by the Biot-Savart law. Herein we presumed that the wires are infinitely long. These currents were calculated according to the RF phase encoding method, aimed to produce a linear varying phase mapping along with one axis. By using the constructed measurement device, the experimental phase profile could be obtained. It was found that a linear spatial phase variation occurs along the axis, with the RF birdcage-coil setup.

By comparing the theoretical phase map with the experimental, the difference was quantified. Then, we could reach the conclusion that the proposed RF coil design works as predicted by theory.

ACKNOWLEDGMENTS

There are a number of individuals who support and encourage me during this graduate program, which help me make this work possible.

First and foremost, I wish to thank Prof. Gordon E. Sarty and Prof. Michael P. Bradley for their roles as my supervisors. I am grateful for the time and efforts they devoted in my research and program. Without their guidance, this dissertation would not have been possible. I could not express enough thanks to my advisory committees, Prof. Jonathan Sharp from University of Alberta, Prof. Paul Babyn from medical imaging at U of S, Prof. Akindele G. Odeshi from mechanical engineering and my external examiner Prof. Glenn Hussey from physics for their useful comments and insightful questions on this thesis.

I am grateful to all the professors who I have taken courses from, Prof. Safa Kasap, Prof. Anh V. Dinh and Prof. Nurul A. Chowdhury for their sharing professional knowledge with me. In addition, my sincere thanks go to all my classmates and friends in the Biomedical Engineering Division and Department of Physics & Engineering Physics, who makes my student life joyful, including but not limited to: David McColl and Debjyoti Basu from Physics Plasma lab; Michael Dorma, Mitchell Tallon and Graeme Scott; Wagemakers Andrew, Eric Peach for their assistance on NI LabVIEW which contributes to my project in the early time, even though this part is not applied in this thesis; Somaie Salajeghe and her husband Majid Nazemi, my friends who accepted (so to speak) my never-ending talking about the vision of the future of the medical industry.

Thanks to my family for their endless love and support throughout my life. Their unwavering support is what allowed me to achieve my goals.

TABLE OF CONTENTS

LIST OF TABLES

LIST OF FIGURES

LIST OF ABBREVIATIONS

Anisotropic Magnetoresistive (AMR)

Analog to Digital (A/D)

Common-mode rejection ratio (CMRR)

Computed tomography (CT)

Compact MRI Field Mapper (field-mapper)

Digital voltage multimeter (DVM)

Data acquisition (DAQ)

Giant Magnetostrictive (GMR)

Ground pin (GND)

HP3468A digital multimeter (HP3468A-DVM)

Magnetic field imaging (MRI)

Nuclear magnetic resonance (NMR)

Operational Amplifier (op amp)

Output Voltage pin of the Hall Effect sensor (Vout-s)

Parts per million (ppm)

Power supply Voltage of the Hall Effect sensor pin (Vcc-s)

Signal-to-Noise Ratio (SNR)

CHAPTER 1

INTRODUCTION

1.1 MRI

Magnetic Resonance Imaging (MRI) is an imaging technique that uses nuclear magnetic resonance (NMR) for the production of images of objects, especially living tissue.

Compared with X-ray based computed tomography (CT), MRI offers significant advantages, including lack of the ionizing radiation and the ability to acquire data in arbitrary orientations ([1] - [2]).

MRI uses a powerful magnetic field to align the magnetization of atomic nuclei, generally hydrogen nuclei, in the body. Radiofrequency (RF) pulses are applied to alter the alignment of the magnetization. This causes the nuclei to produce a rotating magnetic field which is detectable by RF pick-up coils. Finally, an image is reconstructed from the recorded information.

This thesis evaluates the design of an RF coil intended for use in MRI based on recent RF-encoding methods. The idea behind RF encoding is that spatial phase variation in the magnetic field of the RF transmission can be used to encode spatial information in the MRI signal instead of using gradient magnetic fields. Since RF encoding is essentially a k-space method, analogues of many conventional pulse sequences are possible. Note that k-space is the spatial frequency space.

1.2 Research objective

The main objective of this thesis was to obtain experimental phase mapping information of the magnetic field produced by an RF encoding birdcage-coil current.

Specifically, the research had following objectives:

1. To construct a DC birdcage assembly;

2. To set up a magnetic field measurement system;

3. To measure the magnetic field phase gradients of the DC birdcage-coil with the appro--priate RF encoding currents in the coil leg.

1.3 Organization of the thesis

The main objective of this thesis is to measure the magnetic field produced by the RF encoding birdcage coil current. The construction of a measurement system was required to meet the main objective. Since the construction of the measurement system included the amplifier design for measurement signal conditioning, a series of experimental calibrations is also covered.

The thesis is divided into five chapters.

Chapter 1 introduces the motivation, objective and the organization of the thesis.

Chapter 2 gives details of the RF encoding technique, and introduces the reader to the birdcage coil design and the Biot-Savart Law. The simulation of the magnetic field produced by the RF encoding birdcage current is discussed.

Chapter 3 gives details of the experimental work, including the design procedure for each part of the measurement device.

Chapter 4 describes a series of experiments to calibrate the sensor and the amplifier design of the measurement system. Additionally, the results of the phase mapping within the DC birdcage-coil assembly are presented.

Chapter 5 summarizes the work done and discusses potential work for future researchers.

CHAPTER 2

A BIRDCAGE COIL FOR RF ENCODED MRI

This chapter provides background on a recently described MRI image encoding method based on RF phase. The new method encodes spatial information in the MRI signal using the B_1 field of transmitted radiofrequency (RF) with a spatially dependent magnetic field phase. The published details of the RF encoding coil design are limited and none of the commercially available MRI RF coils can produce a linear spatial phase variation of the RF magnetic field. For RF coil design, a commonly-used one is a cylindrical birdcage coil design. Using the target field method [3], the current required for RF encoding within a birdcage-like RF coil can be calculated (In this thesis, the required current is called the RF encoding birdcage current). The magnetic field produced by the RF encoding birdcage current was mapped in the experiments, described in Chapter 3 and 4, to verify if the expected magnetic field was produced in a DC test birdcage coil. The details of the concepts and the applications of the MRI can be found in various MRI textbooks [1], [2], [4]–[11].

2.1 RF Encoded Imaging

2.1.1 Background

The RF encoding imaging method was first proposed in [12] and described in more detail in a subsequent patent [13]. The novelty of this new encoding method is based on using an RF phase gradient as an alternative approach to main field (B_0) imaging. Potential applications

could be lower-cost, simpler and silent MRI systems. The idea is to use the magnetic field component of the transmitted RF B_1 with spatial variation of the phase Φ:

$$\Phi = \tan^{-1}\left(\frac{B_{1y}}{B_{1x}}\right) \tag{2.1}$$

where B_{1x}, B_{1y} denotes x and y component of the magnetic field B_1 respectively.

Since magnetic resonance imaging techniques were first commercialized in the 1970s, MRI hardware has consisted of five main sub-systems [14] :

(1) A Static magnetic field B_0 which should be as uniform as possible;

(2) Gradient magnetic field generator systems;

(3) A radiofrequency (RF) system which includes the RF amp, RF channels, an RF coil etc;

(4) The computation/control systems;

(5) The auxiliary parts, like user interface software, system disk and console etc.

If one sub-system could be eliminated, the cost for the whole equipment might be substantially reduced and the whole MRI scanner system would be substantially different from existing systems. Such new MRI designs could potentially open up new markets for lower-cost and more compact MRIs.

2.1.2 Encoding method summary

Current commercially available MRI methodology uses a set of electromagnetic coils to produce three linear magnetic gradient fields to add on top of the static field B_0 (main field).

This conventional imaging method is a frequency encoding method. Adding the field gradients modifies the resonant frequency ($\omega = \gamma \mathrm{B}_0$, γ is the gyromagnetic ratio) with a total field of $\mathrm{B} = \mathrm{B}_0 + xG_x + yG_y + zG_z$. G_x , G_y , G_z are the three linear field gradients along with x, y, z axis, respectively.

A typical magnetic field gradient system hardware set up requires waveform generation electronics, high-power amplifiers, suitable filters, cables and heavy-water-cooled self-shielded gradient coils [12]. In addition to this limitation, rapidly switched gradient coil currents produces loud noise and vibration [15]. In practice, in order to avoid painful or potentially harmful nerve stimulation, the switching rates are also limited [12].

Encoding method	Static field	RF field(B1 field)	Gradient type
Frequency encoding	$B_0 + x \cdot G_X$	B_1	Main Field
Rotating frame imaging(Casanova's method)	B_0	$B_1 + x \cdot G_{1X}$	RF magnitude
TRASE method	B_0	$B_1 \exp(ix \cdot G_{1X})$	RF phase

Table 2.1: A comparison between three MRI encoding methods based on [12].

The originally proposed RF encoding imaging, Transmit Array Spatial Encoding (TRASE), produced images encoded through the manipulation of RF transmission without gradient coils. The idea behind RF encoding is that we use spatial phase variation in the RF transmission to encode spatial information in the MRI signal instead of using gradient magnetic fields. Another earlier silent imaging strategy based on using magnitude gradients in the transmit RF field was proposed by Hoult [16]. A barrier to its more wide spread adoption is the requirement for high peak RF power and slow scanning speed as mentioned in Sharp and King's original TRASE paper [12]. A more recent high-speed rotary frame imaging method was

proposed by Casanova et al [17]. This has been demonstrated to work well for a small sample and be able to excite a single slice selectively. But in the view of Sharp and King [12], Casanova's method would not allow sufficient flexibility and rapid access to the third spatial dimension. Table 2.1 shows a comparison between these three MRI encoding methods.

2.1.3 RF encoding in 1D

Conventionally, the Lauterbur [18] and Mansfield [19] approach to MRI has been to produce linear gradients and add them to the main magnetic field, driven with a high–current waveform, in order to modify the nuclear magnetic resonance (NMR) resonance frequency. The principle is illustrated by:

$$\omega(x, y, z, t) = -\gamma \cdot \left(B_0 + xG_x(t) + yG_y(t) + zG_z(t) \right) \tag{2.2}$$

where $G_x = \frac{\partial B_z}{\partial x}$, $G_y = \frac{\partial B_z}{\partial y}, G_z = \frac{\partial B_z}{\partial z}$ are the three linear field gradients; t represents time.

k is the spatial frequency coordinate (cycle/m), which is used to collect all the data needed for a full image (See Equation (2.3)).

$$\vec{\mathrm{k}}(\mathrm{T}) = \frac{\gamma}{2\pi} \int_0^T \vec{G}(t) dt \tag{2.3}$$

The RF encoding approach is based on special RF coils that produce linear phase gradients in the magnetic field of the RF field, B_1. A B_1 suitable for RF encoding is given by the following, assuming zero phase at $\vec{\mathrm{r}} = 0$:

$$\vec{\mathrm{B}}_1 = \left| \vec{\mathrm{B}}_1 \right| e^{i\phi_1(\vec{\mathrm{r}})}, \text{ where } \phi_1(\vec{\mathrm{r}}) = 2\pi \vec{\mathrm{k}}_1 \cdot \vec{\mathrm{r}} = \vec{G}_1 \cdot \vec{\mathrm{r}} \tag{2.4}$$

The $\vec{k}_1$ in Equation (2.4) describes the direction and degree of the twist inherent in the phase of RF field, which helps us characterize the RF field. $\vec{G}_1$ is the phase gradient (radians/m). Note that the traditional RF coil is with uniform phase so that $\vec{k}_1=0$.

Given an initial longitudinal magnetization, M_0, applying a 90°_{-Y} RF excitation pulse (90°_{-Y} represents a 90 degree pulse which the net magnetization vector rotates 90 degrees and rotates about the y-axis) with an RF phase gradient coil, we get the transverse magnetization of M_{xy} :

$$M_{xy} = M_0 e^{i\phi(\vec{r})} = M_0 e^{i2\pi\vec{k}_1\cdot\vec{r}} \tag{2.5}$$

The M_{xy} in Equation (2.5) is the component of the net magnetization vector located at right angles to the main magnetic field. Precession of the transverse magnetization at the Larmor frequency (ω) generates the signal. Without an RF field, transverse magnetization decays to zero with a characteristic time constant of T_2 and the value drops from the maximum to about 37% of its original value in a time T_2 [20].

Equation (2.5) shows that excitation with a $\vec{B}_1$ gradient results in a spatially dependent spin state M_{xy} phase. The spin system is directly excited to the k-space coordinate $\vec{k}_1$. Conversely, the phase gradient coil will receive a signal with a k-space shift of $-\vec{k}_1$. See Figure 2.1 below.

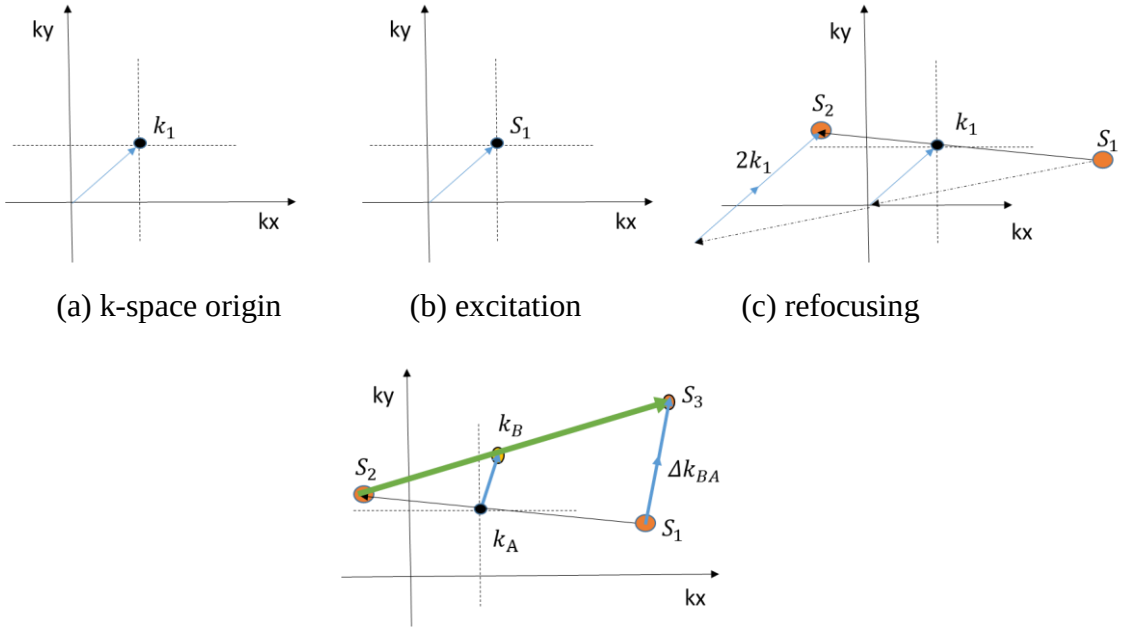

(a) k-space origin (b) excitation (c) refocusing

(d) translation

Figure 2.1: K-space properties for a spin state excited with RF phase gradient fields. Extracted from the Sharp's and King's paper [12].

As shown in Figure 2.1, the phase gradient excitation result is presented as a point in k-space, where $\vec{k}_1$ is referred to as the 'k-space origin'. Excitation using the phase gradient field results in excitation to the point k_1.

When applied with an RF phase gradient field, a 180° RF pulse rotates initial transverse magnetization M_{xy}^{-} around the $\vec{B}_1$ field direction given by $\phi(\vec{r})$ to M_{xy}^{+}; then the post-spin echo transverse magnetization becomes:

$$M_{xy}^{+} = M_{xy}^{-*} e^{i2\phi_1(\vec{r})} = M_{xy}^{-*} e^{i2\pi[2\vec{k}_1 \cdot \vec{r}]} \tag{2.6}$$

Equation (2.6) determines the spin state after an RF-encoding pulse. In k-space, where $\vec{k}_+$ $\vec{k}_-$ represents the phase before and after RF-encoding pulse, respectively.

$$\vec{k}_+ = -\vec{k}_- + 2\vec{k}_1 \tag{2.7}$$

We can use Equations (2.6) and (2.7) as characterizations of the effect of RF phase gradient refocusing pulses to construct an echo train, with each subsequent echo having a different k-space encoding. Note that for an RF encoding echo train, the phase evolves discretely at each refocusing pulse.

Consider a transmit array coil capable of producing one of two RF phase gradients, A and B. The two gradient fields are selected alternatively to produce refocusing pulses:

$$90_A - 180_A - M_1 - 180_B - M_2 - 180_A - M_3 - 180_B - M_4 - 180_A - M_5 - 180_B \ldots \quad (2.8)$$

where M_i denotes measured magnetization M_{xy} for the i th echo.

Based on Equations (2.6) and (2.7) for RF phase gradient refocusing pulses, for a BA pair echo train, the spin will receive a phase increment of $2\left(\vec{k}_B - \vec{k}_A\right)$, in terms of k-space, from each pair of pulses. Note that, following Equation (2.3), the spin phase is proportional to the spatial position when moving down the BA pair echo train.

As shown in Figure 2.1(c), refocusing an arbitrary spin-state using the phase-gradient field results in refocusing about $\vec{k}_1$. The effect of two successive refocusing pulses with different field 'k-space origins', $\vec{k}_A, \vec{k}_B$, is to translate arbitrary k-space point by $\Delta\vec{k}_{BA} = 2\left(\vec{k}_B - \vec{k}_A\right)$ as shown in Figure 2.1(d).

In summary, the key to RF encoded MRI, according to Sharp and King [12], is to refocus using RF phase gradients repeatedly, allowing the signal states and k-space trajectory to accumulate to higher k-space values.

2.1.4 RF encoding in 2D and 3D

RF-encoding can be extended to 2D imaging by adding a third non-collinear RF phase gradient $\vec{G}_C = 2\pi\vec{k}_C$, so that the 2D k-space plane can be traversed. Similarly, four fields are sufficient for 3D imaging, as long as the field gradients are all non-collinear and non-coplanar. Since RF encoding is a k-space-based technique, pixel size is proportional to the reciprocal of the sample k-space extent. Additionally, RF encoding can also be combined with time-domain multiplexing acceleration methods and slice selection methods [12], [13], [21], [22]. These aspects will not be discussed further here.

2.2 Birdcage Coil

2.2.1 MRI RF coil overview

In MRI systems, radiofrequency (RF) coils, also known as RF resonators and RF probes, are key components. The majority of MRI systems are designed to detect the nuclear spin flip resonance of atomic hydrogen $^{1}\mathbf{H}$ (i.e. protons). The reason for this is that water is the most abundant compound in the human body, constituting a major portion of the most medically interesting structures (e.g. brain tissue).

The main purpose for the RF coils in an MRI machine is to generate and/or detect RF oscillations at the Larmor spin precession frequency $f = \omega / 2\pi$ where

$$\omega = \gamma B . \tag{2.9}$$

In this equation, γ is the gyromagnetic ratio of the nucleus which is undergoing spin precession. For hydrogen nuclei $\gamma = 42.6\ MHz/T$. The RF coils are used to excite the hydrogen nuclei in the sample object, or to pick up the RF signal emitted by the hydrogen nuclei at the spin precession frequency. RF coils may be categorized into three types: RF transmit only coil, RF receive only coil or an RF transmit/receive coil.

In order to obtain high quality MRI images, the RF coil must satisfy some basic requirements:

1. When used as a transmit coil, an RF coil must be able to produce a homogeneous B_1 field in the intended field of view (FOV), so that the nuclei can be excited uniformly. (The B_1 field is the magnetic field of the RF pulse generated by RF transmit coil, whose effective direction is perpendicular to the direction of the B_0 field.)

2. When used as a receive coil, an RF coil must be able to pick up RF signals with the same gain from any points in the FOV. The coil must also have a high signal-to-noise ratio (SNR).

2.2.2 RF coil design

The B_1 field direction is not the same as the B_0 field direction, so RF coil design is different for both gradient coil design and shim coil design.

An imaging coil must resonate, or efficiently store energy, at the Larmor frequency. All imaging coils are composed of an inductor, or inductive elements, and a set of capacitive elements. The resonant frequency, ω, of an RF coil is determined by the inductance (L) and capacitance (C) of the inductor capacitor circuit:

$$\omega = \frac{1}{\sqrt{LC}} \tag{2.10}$$

RF coils for MRI can be grouped into two different classes: volume coils and surface coils. Volume coils surround the imaged object while surface coils are placed adjacent to the imaged object. There is another type, the internal coil [23], which is designed to record information from regions outside of the coil, such as a catheter coil designed to be inserted into a blood vessel [24]. Examples of internal coils include an implantable coil [25] and an intravascular coil [26].

2.2.2.1 Surface coil

Surface coils [27] are designed to provide a very high RF sensitivity over a small region of interest, which are placed directly over the anatomy of interest. Surface coils are usually smaller than volume coils and can be optimized for the specific region of interest. Surface coils have poor RF homogeneity (B_1 field homogeneity), so they are mainly used as RF receive only coils.

2.2.2.2 Volume coil

Volume coils are designed to provide a homogeneous RF excitation across a large volume. Examples include Helmholtz coils, saddle coils, transverse electromagnetic (TEM) coils [28], Alderman-Grant coils [29] and birdcage coils. Figure 2.2 shows an example of a birdcage coil design. Volume coils require greater RF power because their size is large. Thus they are often driven in quadrature, in order to reduce by a factor of two the RF power requirements. Most clinical MRI scanners include a built in volume coil to perform whole-body imaging, and

smaller volume coils have been constructed for the head and other extremities [30]. The RF homogeneity of volume coils is highly desirable for transmission but is less ideal when the region of interest is small. The RF coil may receive noise not only from the area of interest, but from the entire enclosed whole body [31]. The birdcage coil is the most routinely and commonly used volume coil design.

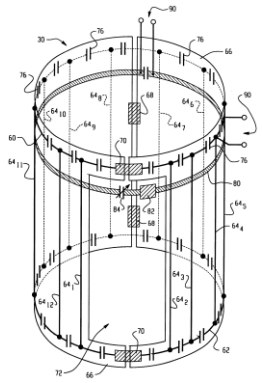

Figure 2.2: Diagram of an example of the birdcage coil. Referred from Fig 1 from the US patent US6316941 B1[32].

2.3 Biot-Savart Law

Magnetic fields are due to electric currents. The Biot-Savart Law enables the calculation of the vector magnetic field $\vec{B}(x,y,z) = \vec{B}(\vec{r})$ at an arbitrary location (the "field point") $\vec{r} = (x,y,z)$ due to a current I flowing along a wire described by differential line elements $d\vec{\ell}'$. The magnetic field at an arbitrary field point is given by *vector sum* of the contributions from the individual current elements. With reference to the geometry shown in Figure 2.3(a), the total field is found by integrating over all current carrying wire elements $Id\vec{\ell}'$, as follows:

$$\vec{B}(x,y,z) = \vec{\mathrm{B}}(\vec{\mathrm{r}}) = \frac{\mu_0 I}{4\pi}\int_C \frac{d\vec{\ell}' \times \vec{R}}{\left|\vec{R}\right|^3} \tag{2.11}$$

where I denotes the current; $d\vec{\ell}'$ denotes a vector whose magnitude is the length of the differential element of the wire in the direction of the current; μ_0 is the permeability of free space, $\mu_0 = 4\pi \times 10^{-7}$ T·m /A; $\vec{\mathrm{R}}=\vec{r}-\vec{r}'$ is the vector from the location $\vec{r}' = (x', y', z')$ of the wire current element $Id\vec{\ell}'$ to the location $\vec{r} = (x, y, z)$ of the field point. $\vec{B}$ (in units of Tesla or Weber/m^2) is the resultant magnetic induction field vector, and is also referred to as the magnetic flux density. The related quantity $\vec{H} = \vec{B} / \mu_0$ is referred to as the "magnetic field" in engineering work, and has units of A/m. $\vec{H}$ is widely used in electromagnetic engineering, but $\vec{B}$ is more convenient for use in magnetic resonance applications.

For this work, it was necessary to compute the magnetic field vector at an arbitrary point *P* due to the currents in a *birdcage-style* array (see Figure 2.2) of eight parallel current-carrying wires which are arranged in a circle around a central axis. This wire array is depicted schematically adjacent to Table 2.2. Computation of the field was carried out using the expression for the magnetic field due to a long straight wire; for the relevant geometry see Figure 2.3(b). The field in this case can be computed by direct integration using the Biot-Savart law, but the computation is more easily done using Ampère's law, as follows:

$$\int_{loop} \vec{B} \cdot d\vec{l} = \mu_0 I_{in} \Rightarrow B \cdot 2\pi a = \mu_0 I_{in} \Rightarrow \vec{B} = \frac{\mu_0}{2\pi} \frac{I}{a} \hat{\phi} \tag{2.12}$$

where a denotes the distance between the coil wire and the field point *P*.

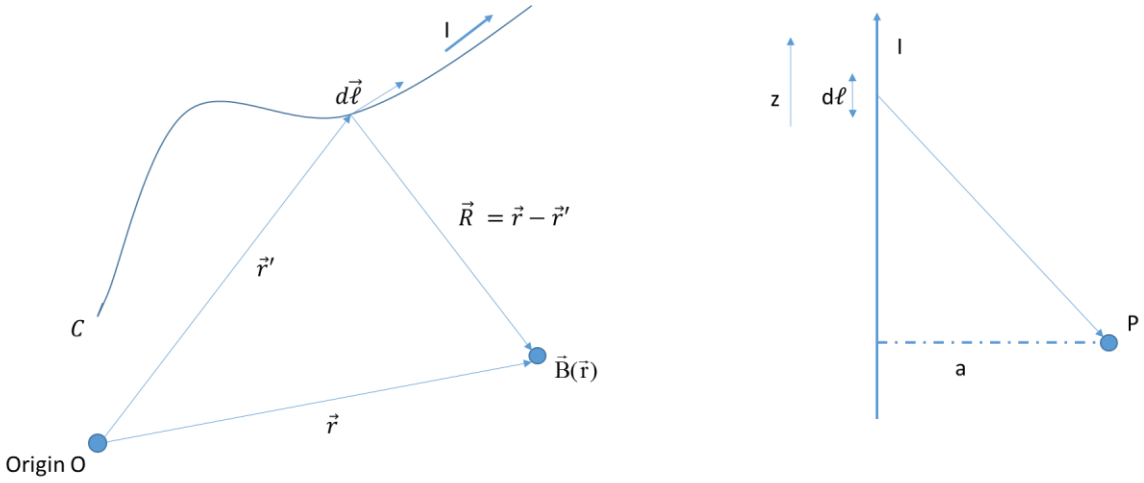

(a) (b)

Figure 2.3: (a) Geometry of the Biot-Savart law for a current I flowing in a wire of arbitrary configuration. The vector $d\vec{\ell}$ is a differential length element of the wire, oriented in the direction of current flow. μ_0 is the permeability of free space, $\mu_0 = 4\pi \times 10^{-7}$ T·m/A ; $\vec{R}$ denotes the displacement vector from the wire element to the point at which the field is being computed, and $\vec{B}$ denotes the magnetic flux density or magnetic induction field vector at the field point. (b) Geometry for the case of a long straight wire; a denotes the distance between the coil leg and the field point P.

2.4 RF encoding birdcage coil current

Table 2.2(a) gives the calculated wire currents for an 8-leg birdcage-style coil; note that the long axis of the assembly is oriented along the Z axis, with the X-Y plane being perpendicular to this; the schematic adjacent to Table 2.2(a) shows an X-Y section of the 8-wire configuration. The leg currents were computed by Prof. Gordon Sarty, using the target field method; this configuration is described further in a 2016 Canadian patent application [33]. It is important to note that these currents can be scaled by a constant factor, since the spatial phase* of the magnetic field in the X-Y plane $\theta = \arctan(\frac{B_X}{B_Y})$ is unchanged if both field

components B_X and B_Y are scaled by the same factor. *Note that in this section the spatial phase angle θ is defined in a non-standard way, relative to Y axis, as shown in Figure 2.4.

	$Ga=\pi$	$Ga=2\pi$	$Ga=3\pi$
i_1	-0.699	-0.944	-0.567
i_2	0.384	-0.989	-3.951
i_3	2.159	4.597	9.760
i_4	0.384	-0.989	-3.951
i_5	-0.699	-0.944	-0.567
i_6	-0.544	-0.265	-0.039
i_7	-0.441	-0.164	-0.023
i_8	-0.544	-0.265	-0.039

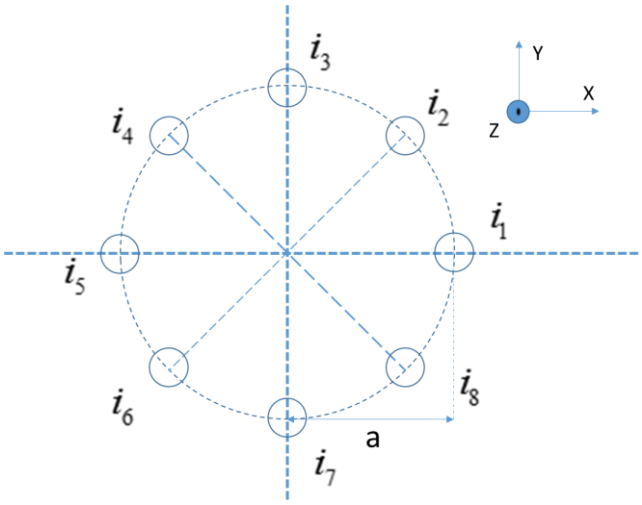

Table 2.2: (a) Computed coil leg currents in Amperes, calculated to give a uniform amplitude target field with a linearly varying spatial phase. *G* denotes the phase gradient, in units of radians/meter. (b) *a* is the radial distance in meters from the center of the cage assembly to the center of each current-carrying wire.

Additionally, note that the given currents are obtained not based on the ideal B_1 field. It is the based on a target field approach with the target field being the ideal linearly varying spatial RF phase. Note that the target field amplitude was chosen to be uniform for the calculated currents given in Table 2.2. Take the case $Ga = \pi$ as example.

The ideal B_1 field can be given as :

$$\vec{B}_1 = \vec{B}_1(x) = B_X(x)\vec{i} + B_Y(x)\vec{j} = \left|\vec{B}_1\right|\sin\theta\vec{i} + \left|\vec{B}_1\right|\cos\theta\vec{j} \tag{2.13}$$

For 1D RF encoding, substitute $\theta(x) = Gx$ into Equation (2.13) to obtain

$$\vec{B}_1 = \left|\vec{B}_1\right|\sin\theta\vec{i} + \left|\vec{B}_1\right|\cos\theta\vec{j} = \left|\vec{B}_1\right|\sin(Gx)\vec{i} + \left|\vec{B}_1\right|\cos(Gx)\vec{j} \tag{2.14}$$

When $\theta(a) = G \cdot a = \pi$, the B_1 field at the point a and the point $-a$ become:

$$\vec{B}_1(a) = \left|\vec{B}_1\right|\sin(\pi)\vec{i} + \left|\vec{B}_1\right|\cos(\pi)\vec{j} = -\left|\vec{B}_1\right|\vec{j}$$
$$\vec{B}_1(-a) = \left|\vec{B}_1\right|\sin(-\pi)\vec{i} + \left|\vec{B}_1\right|\cos(-\pi)\vec{j} = -\left|\vec{B}_1\right|\vec{j} \quad (2.15)$$

Figure 2.4(a) shows the schematic of the magnetic field varying with a constant phase gradient G in the x direction as shown in Equation (2.14). Note the non-standard definition of the spatial phase angle θ (defined with respect to the Y axis).

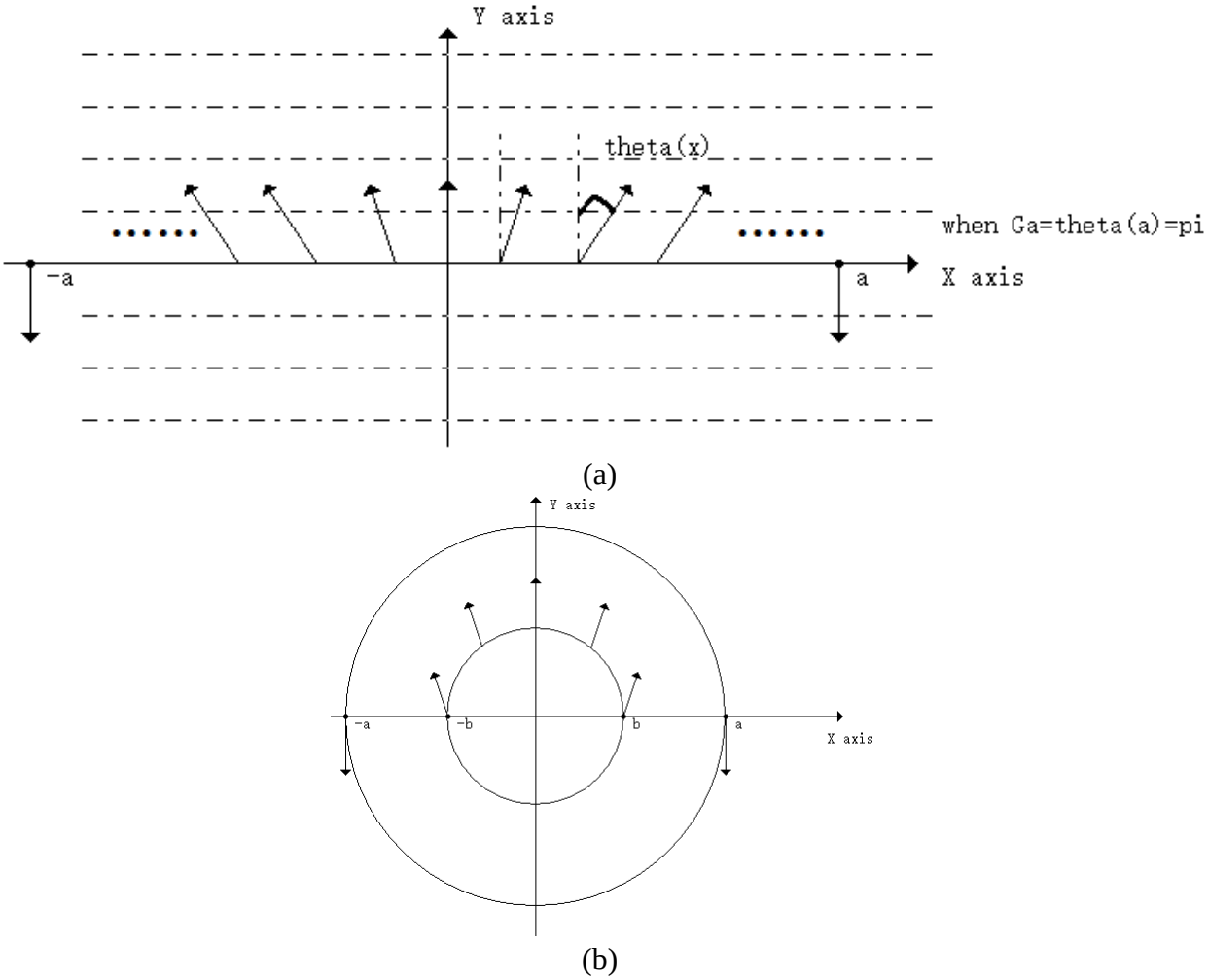

Figure 2.4: (a) Illustration of the B_1 ideal field. (b) Illustration of the B_1 generated field. The target field is at $r = b$.

The equation for the magnetic field due to a long straight wire (Equation (2.12)) was used to compute the vector magnetic field $\vec{B}(x, y, z)$ produced by the leg-currents $i_1, i_2, \ldots\ i_8$ given in

Table 2.2(a). The computation was carried out using Matlab [34]–[41]. The resulting amplitude $\left|\vec{B}\right|$ and spatial phase $\theta = \arctan(\frac{B_X}{B_Y})$ for the three different cases ($Ga = \pi, 2\pi, 3\pi$) are shown in Figure 2.5.

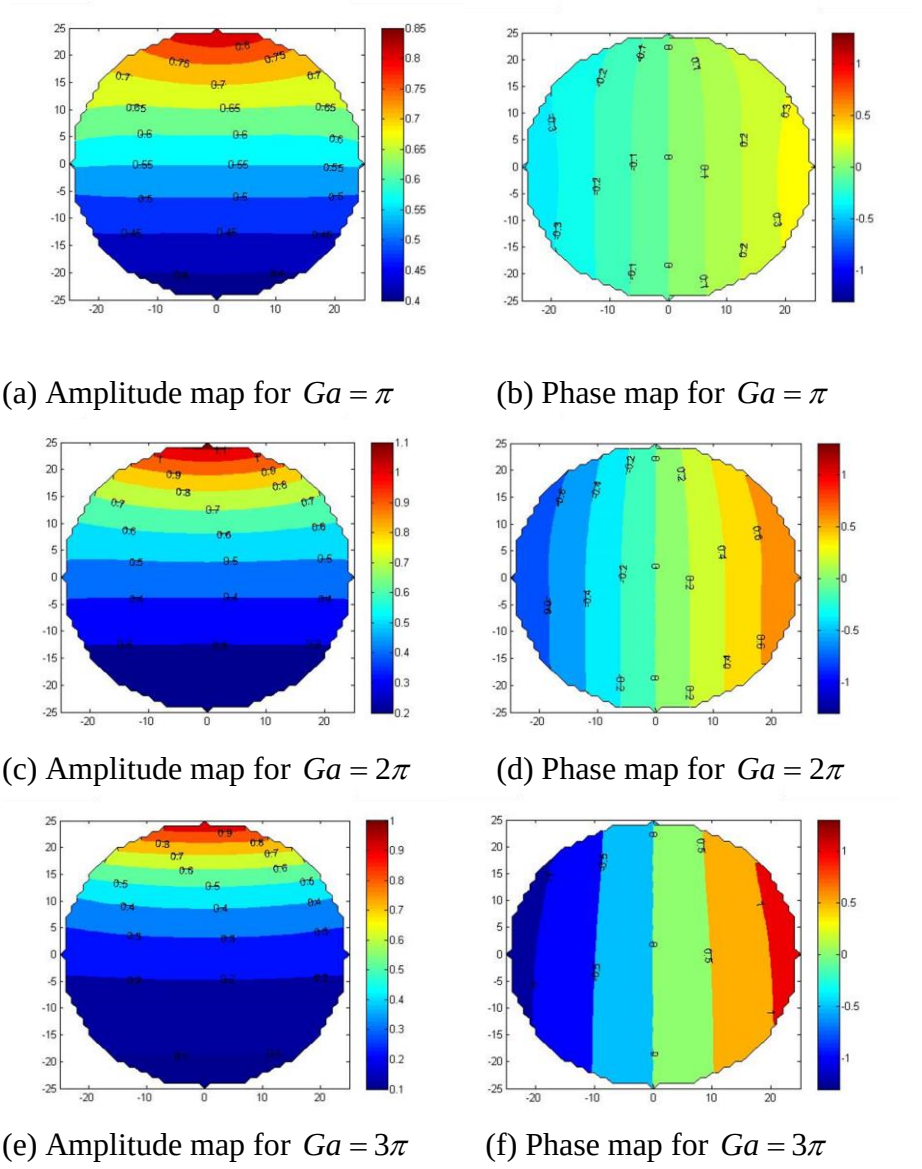

(a) Amplitude map for $Ga = \pi$ (b) Phase map for $Ga = \pi$

(c) Amplitude map for $Ga = 2\pi$ (d) Phase map for $Ga = 2\pi$

(e) Amplitude map for $Ga = 3\pi$ (f) Phase map for $Ga = 3\pi$

Figure 2.5: The simulation results of the magnetic field produced by the currents of Table 2.2. Unit: Gauss in (a)(c)(e); Unit: 1 in (b)(d)(f).

However, the phase map presented in Figure 2.5 is not the ideal B_1 field map. It is the ideal B_1 field computed on a circle of radius *b*, where *b* is chosen to be less than the radius

a=0.105 meter of the circular array of birdcage wire legs. (See Figure 2.4(b)) The radius b is set to be 0.020 meter. Note that the experimental measurements of the spatial phase (discussed in Chapter 4 and 5) were carried out only within the target field radius ($r = b$).

The comparison of the magnetic field phase profiles in case $Ga = \pi$ is presented in Figure 2.6. The phase ranges from $-\pi$ to $+\pi$ in Figure 2.6(a); the Figure 2.6(b) shows the phase map for the circle of radius $r = b$.

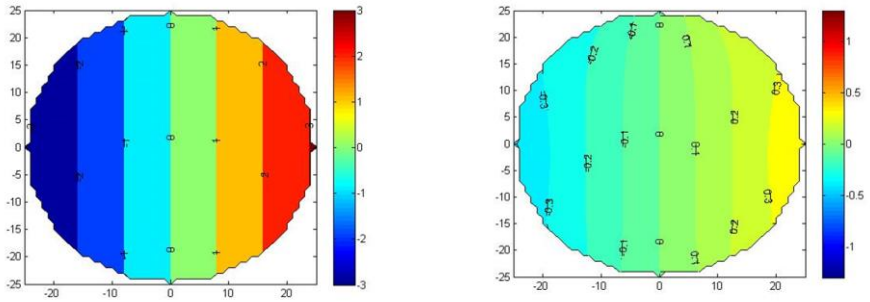

(a) Phase map for $Ga = \pi$ (ideal field) (b) Phase map for $Ga = \pi$ (b-circle area)

Figure 2.6: Comparison of the phase map between the ideal field and the simulated field for the case $Ga = \pi$ where $G = 29.9199$ **radian/meter** , $a = 0.105$ **meter** , $b = 0.020$ **meter** .

CHAPTER 3

EXPERIMENTAL SYSTEM

3.1 Introduction

This chapter describes the experimental set-up of a DC-driven 8-leg birdcage coil, with current legs/wires on a circle of diameter $2a$ = 0.100 meter, as well as a custom-made magnetic field probe based on a Hall Effect sensor. This system was used to measure the vector magnetic field in the plane perpendicular to the cage assembly long axis within a scanning circle of radius r = 0.025 meter. This scanned circle radius is slightly larger than the target field circle of radius b = 0.020 meter. From the measured vector magnetic field data, a map of the spatial phase of the magnetic field within the circle of radius r = 0.025 meter was obtained under different drive conditions (i.e. different drive currents, $i_1, i_2, \ldots\ i_8$, in the birdcage assembly legs).

3.2 Birdcage setup

In this section, the design of the birdcage coil setup is discussed. An eight-rod birdcage style coil assembly was constructed. The current-carrying rods were made of aluminum, a paramagnetic material with high conductivity. The aluminum is only weakly paramagnetic, which results in minimal field perturbation. Figure 3.1 shows the basic design.

In the original design, the circle diameter was chosen to be 210 mm (to match the value of $2a = 210$ mm chosen in Section 2.4). However, due to power supply current limits (10 Ampere maximum), the total magnetic field generated in the birdcage design was too small to

detect and it was below the minimum detectable value for the magnetic field sensor (see Section 3.3.1), for the case that the original design diameter of 210 mm. Therefore, to ensure a reasonable magnetic field signal that could be detected and processed by the Hall Effect sensors, the final version for the circle diameter was chosen to be $2a$ = 100 mm. This choice required a re-scaling of the drive currents for the cage bars (See Section 4.2.2).

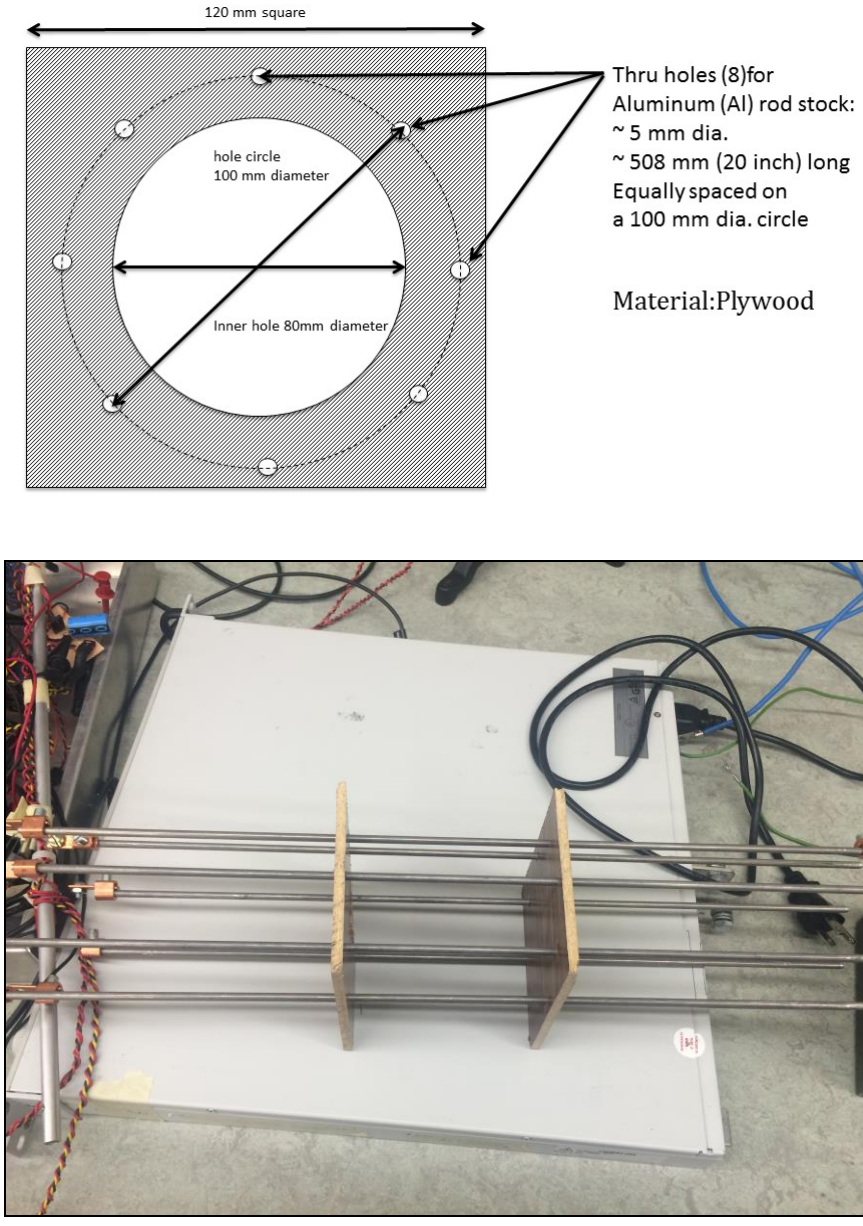

Figure 3.1: Demonstration of the birdcage coil setup. There are 8 holes for aluminum (Al) rod wire legs equally spaced on the $2a$ = 100 millimeter diameter circle. Each leg is around 20 inch

long (508 mm). Each hole is approximately 5 mm in diameter. The diameter of the inner circle in the insulating support plate was designed to be 80 mm, to let the probe in.

3.3 Magnetic field measurement system

This section describes the magnetic field measurement systems, which is used to map the magnetic field inside the birdcage coil. The measurement system must detect the magnetic field, amplify the resulting signal and then convert it to a digital signal so that the data can be analyzed by a computer.

The magnetic field measurement system designed for this work consists of the following four sub-systems:

(1) A probe, to detect and measure components of the magnetic field vector;

(2) Circuits for amplifying the signal; The magnitude of the magnetic field generated by the birdcage coils is around few Gauss and the sensitivity of the sensors we considered is around 1 - 5 mV/Gauss. However, the data acquisition part input voltage range is 5 V. Therefore, amplification is necessary.

(3) A computerized movement system, to drive the probe to the desired position;

(4) Data acquisition hardware and software;

The scope of the experimental system is shown in Figure 3.2. Each sub-system is described in the following sections.

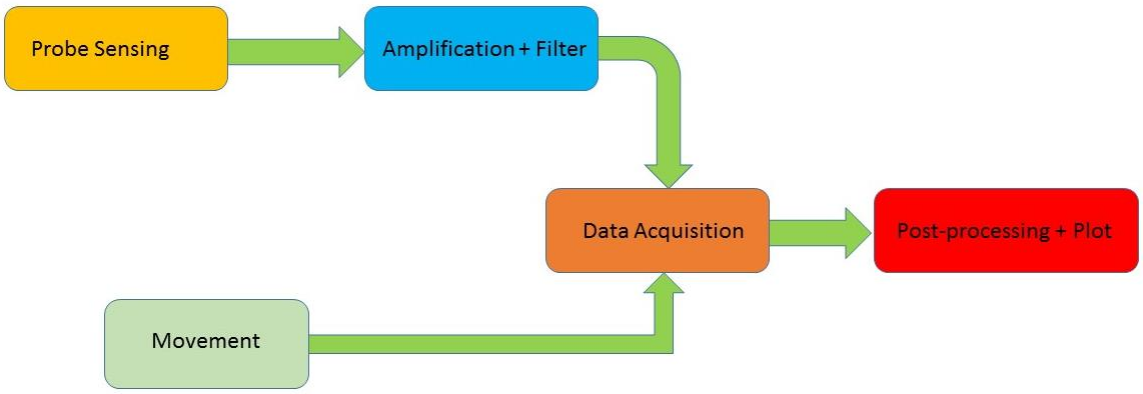

Figure 3.2: The scope of the measurement system.

3.3.1 Magnetic field sensor selection

3.3.1.1 Introduction

Magnetic fields occur in nature (e.g. the Earth's magnetic field) as well as in many applications of electrical technology (e.g. induction motors, electromagnets, particle accelerators, and MRI systems). Between them, these naturally-occurring and technologically-developed magnetic fields cover a very wide dynamic range from microTesla to ~10 Tesla. No single magnetic field sensing technology is capable of measuring the entire range. Therefore a wide variety of magnetic sensing techniques exist for the measurement of the magnetic fields. One way to classify the various magnetic sensors is by the field sensing range [42]–[44]. The minimum detectable magnetic field is an important criterion for sensor selection; Table 3.1 gives typical minimum detectable field levels for a variety of magnetic field sensors.

For the work described in this thesis, since the generated DC magnetic fields are at the Gauss level, a Hall Effect sensor was selected. Hall Effect sensors are inexpensive and

commonly used, and most sealed Hall Effect devices are immune to dust and water as well as vibration, so they are well-suited for use in this moving magnetic probe system.

Magnetic sensor technology	Minimum detectable field (Gauss)
SQUID	10^{-8}
Fiber-Optic	10^{-6}
Optically Pumped	10^{-8}
Search-coil	10^{-8}
Nuclear Procession	10^{-7}
Anisotropic Magnetoresistive	10^{-6}
Flux-gate	10^{-6}
Magnetodiode	1
Magnetotransistor	0.1
Magneto-Optical Sensor	1
Giant Magnetostrictive	0.1
Hall-Effect Sensor	0.1

Table 3.1: Minimum detectable field of the various magnetic sensor technologies (according to [44]). Note for reference that the magnitude of the Earth's magnetic field is about 0.5 Gauss.

The Hall Effect sensors have many advantages as magnetic sensors:

1. Hall Effect Sensors work over a wide temperature range.

2. Hall Effect sensors are made from semiconductor materials which exhibit low carrier density, the Hall voltages are relatively large.

3. Hall Effect sensors provide highly repeatable operation.

4. Hall Effect sensors are not affected by ambient conditions, such as dust, humidity, and vibrations.

5. High speed operation is possible.

6. Hall Effect sensors do not have contact with neighboring mechanical parts.

3.3.1.2 Hall Effect sensor

The Hall Effect sensor is a transducer based on the Hall Effect. The Hall Effect is named after Edwin Hall [45][46], who discovered in 1879 that an electric potential difference (the Hall voltage V_H) develops across a current-carrying conductive plate (also referred to as a Hall bar) when a magnetic field passes through the plate in a direction perpendicular to the plane of the plate. The Hall Effect has its origin in the Lorentz force $\vec{F} = q(\vec{\mathrm{v}} \times \vec{B})$ on a charge q moving in a magnetic field.

Let the charge be moving in the x direction with vector velocity $\vec{\mathbf{v}} = \mathbf{v}\hat{x}$, and let the magnetic field be oriented in the z direction, i.e. $\vec{B} = B\hat{z}$. The moving charge feels an effective electric field $\vec{E} = \frac{\vec{F}}{q} = \frac{q\vec{\mathbf{v}} \times \vec{B}}{q} = \vec{\mathbf{v}} \times \vec{B} = \mathbf{v}\hat{x} \times B\hat{z} = \mathbf{v}B\hat{x} \times \hat{z} = \mathbf{v}B(-\vec{y})$. The magnitude of the Hall voltage across the sample is $V_H = \left|\vec{E}\right| w = vBw$, where w is the width of the sample. This expression is written for a single charge q moving with velocity v. It is conventional to rewrite the expression in terms of the measured current $I = qnvwt$, where n is the carrier concentration and t is the thickness of the Hall bar. Upon substituting $v = \frac{I}{qnwt}$ into the equation for the Hall voltage, we obtain the Hall voltage:

$$V_H = \frac{1}{qnt} IB \tag{3.1}$$

Only the component of the magnetic field which is perpendicular to the Hall bar contributes to the Hall voltage. For a general magnetic field vector, making an angle α with

respect to the surface of the Hall bar, the perpendicular component is $B_z = B\sin\alpha$. Then the general form of the Hall voltage becomes:

$$V_H = \frac{1}{qnt} IB\sin\alpha \tag{3.2}$$

It is conventional to define a Hall coefficient $R_H = \frac{E}{jB}$, where $j = \frac{I}{wt}$ is the current density through the Hall bar. From this we obtain:

$$R_H = \frac{E}{jB} = \frac{vB}{\frac{I}{wt}B} = \frac{vwt}{I} = \frac{vwt}{qnwtv} = \frac{1}{qn} \tag{3.3}$$

The value of R_H in Equation (3.3) depends on the Hall plate material and the temperature since $n = n(T)$.

For engineer selecting a Hall Effect sensor, the most important parameter is the Hall voltage per unit magnetic field, i.e. $\frac{V_H}{B} = \frac{I}{qnt} = \frac{IR_H}{t}$. This is referred as the magnetic sensitivity of the sensor (typically, it given in units of mV/Gauss). Note that the Hall coefficient R_H is an intrinsic property of the material from which the Hall bar was made, whereas the magnetic sensitivity of the Hall Effect sensor is the device property which is dependent on the chosen drive current I and the Hall bar thickness t.

As discussed before, Hall Effect sensors offer a reasonable magnetic sensitivity, excellent linearity, low noise output and a low temperature coefficient in a robust package [47], [48]. For the work described in this thesis, magnetic field sensitivity, the temperature stability, and the device package type were the most important factors.

3.3.1.3 Selection of the Hall Effect sensor

Table 3.2 shows a selection of the Hall Effect sensors which were considered for use in this project. Among them, our decision is the A1301 KUA-T (see Figure 3.3). An earlier selection was the A1302 KLHL-T. However, a few trials showed that a higher magnetic sensitivity was required; therefore, the A1301 KUA-T was selected. In addition, the LH package was not convenient to mount on the cubic probe head (discussed later).

Part Number	Comments (*Sen*=magnetic sensitivity)
AH49E	the temperature is -40~80; sensitivity is a little bit low, just 1.6mV/G
AH49F	B=0 to +-600Gauss, Sen=2.1mV/G
A1363	Programmable IC product; Sen=9.6mV/G
A1324	Sen=5mV/G, out of stock
A1301	Sen=2.5mV/G, low-noise output, 4.5 to 6.0 V operation
A1302	Sen=1.3mV/G, fast power-on time
EQ-430L	Sen=13mV/Gauss, have a rise time and fall time; best-fit, but out of stock
SS490	Ratiometric, around 3.1mV/G
SS39ET	1.4mV/G
SS94A1	5mV/G, out of stock
OHS3151U	2.5mV/G, out of stock
TLE4997E2	programmable,1.25--30mV/G
SS495B-S	3.125mV/G, out of stock
DRV5053CA	23mV/G, out of stock
DRV5053EA	45mV/G, but is not the same package used in this work
DRV5023	digital switch sensor, ignored
DRV5033	omnipolar switch sensor, ignored
A1395	10mV/G, but the Vcc is 3.5V maxium, and 6 pins
A1359	dual track output, A1359LLETR-RP-T, 9mV/G, but 8 pins

Table 3.2: Selection of the Hall Effect Sensor.

Both A1301 and A1302 are continuous-time, ratiometric, linear Hall-effect sensor integrated circuits (Hall Effect sensor ICs). Figure 3.3(a) shows a schematic of the A1301 sensor IC. The Hall-effect sensor IC includes a Hall circuit, a linear amplifier, and a CMOS Class A output structure. Internal gain and offset trim adjustments are made at end-of-line during the manufacturing process.

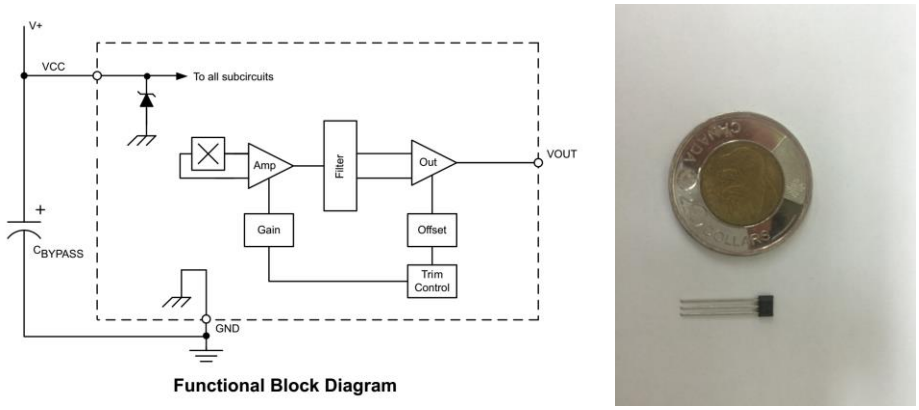

Figure 3.3: Hall Effect sensor A1301 KUA-T. (a) Functional block diagram; (b) Physical package.

The A1301 is capable of sensing the magnetic field and converts it into a voltage output. It is optimized to provide voltage output that is proportional to the applied magnetic field with a sensitivity of 2.5 mV/G (typical) and a linearity of ±2.5%. The fast power-on time and ratiometric rail-to-rail output make it ideal as sensing element for our use. Table 3.3 lists the most important parameters for this work. More detailed description and specifications can be found in the datasheet [49].

Output voltage	Ranges from 0.2 V minimum to 4.7 V maximum
Sensitivity	2.5mV/G (typical)
Linearity	±2.5%
quiescent output voltage	V_{outQ} =2.5V
supply voltage	V_{cc} =5.0V
supply current	I_{cc}=11 mA at maximum
operating ambient temperature	ranges from –40°C to 125°C
power-on time	t_{PO} =5µs
slew rate	4.5V/ µs

Table 3.3: Selected parameters from the specification sheet of the Hall Effect Sensor A1301.

3.3.1.4 Temperature dependence

Figure 3.4 shows that output voltage of the Hall Effect sensor changes with increasing temperature. For this work, with assistance of the voltage meter and air heater, we did a simple test to confirm the Hall sensor's output voltage change over the temperature. The results shows that the Hall Effect sensors worked well at the room temperature.

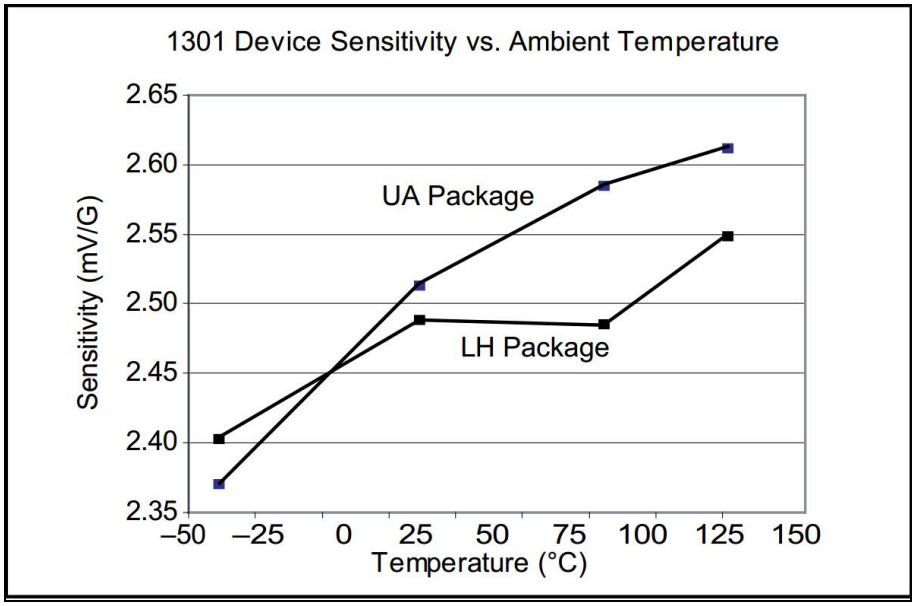

Figure 3.4: A1301 Device Sensitivity vs. Ambient Temperature, extracted from manufacturer datasheet [49].

3.3.1.5 Magnetic field probe

The final static field probe design used Allegro Hall Effect sensors A1301. A number of prototype probe-head designs and probe-bar designs were tried. The process of the probe-head design included three main generations. After experimentations, a two-sensor probe-head was preferred. One Hall sensor measures the Y component of the magnetic field and the other Hall sensor is to measure the Z component of the magnetic field. Note that the coordinate axes used for experimental measurement differ from those used in the theoretical discussion in chapter 2.

Figure 3.5 shows the coordinate system used in all experimental works. Note in a particular that the X axis is aligned with the long axis of the birdcage assembly, while the Y and Z axes are perpendicular to the X axis. The head of the magnetic field probe is built on a small cylinder (length = 80 mm) of delrin which is a non-magnetic material. One end was squared off with a side length of 5 mm, in order to mount the A1301 Hall Effect sensors. The back end of the probe was cut down to a smaller cylinder for mounting purposes. Two small wires were added to the head of the probe for a common GND and common power supply (for sensors) which are needed to operate the sensors. Each pin from each sensor was connected to a wire, which provided the voltage reading. Each sensor was then set in place and secured at the wire with electrical tape to the Delrin piece.

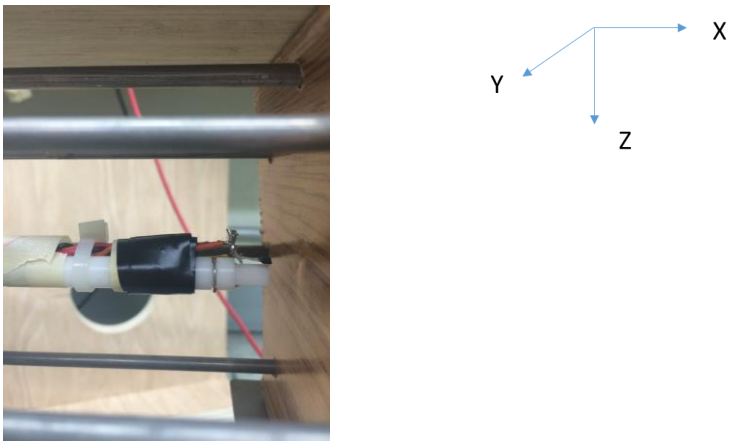

Figure 3.5: Photo of the probe-head design with two Hall sensors. Note the new coordinate system is used for all experimental measurements. In particular, the X axis is aligned with the long axis of the birdcage assembly, while the Y and Z axes are perpendicular to the X axis.

For better responsivity, the magnetic field lines must be perpendicular to the flat face of the A1301 sensor and must be at the correct polarity, which means that the delrin-cylinder-end must be cubic. The probe mount was constructed from a 450 mm long piece of aluminum tubing with a diameter of 9 mm. The wires from each sensor were run along with the aluminum tubing. Tape was needed to set the wires onto the probe bar. Two holes were drilled in the opposite end

that can be used with set screws to mount to the Field-mapper Shapeoko2 machine (discussed later). Figure 3.6 shows the mechanical sketch of the probe and Figure 3.7 shows wiring diagram for the probe head.

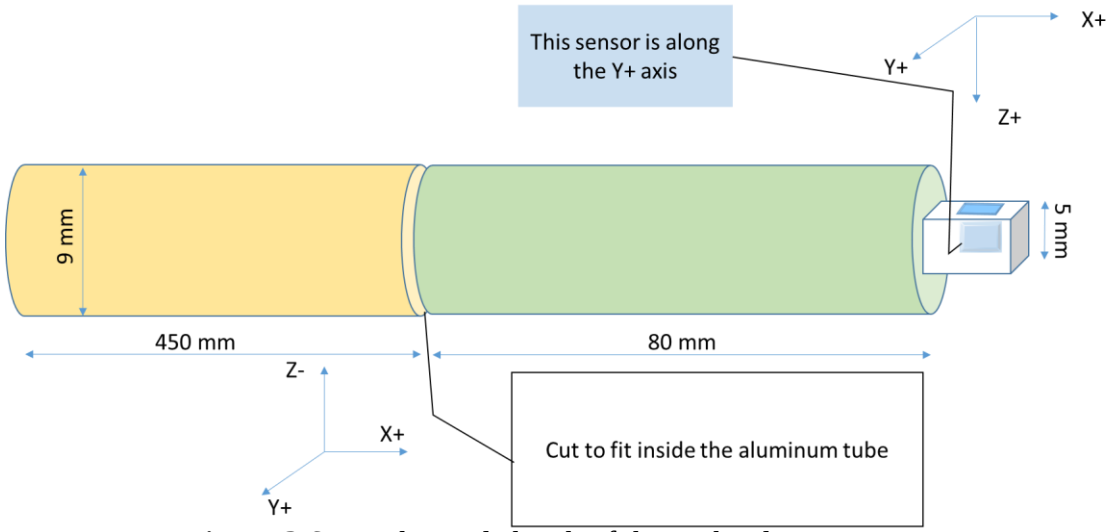

Figure 3.6: Mechanical sketch of the probe-design.

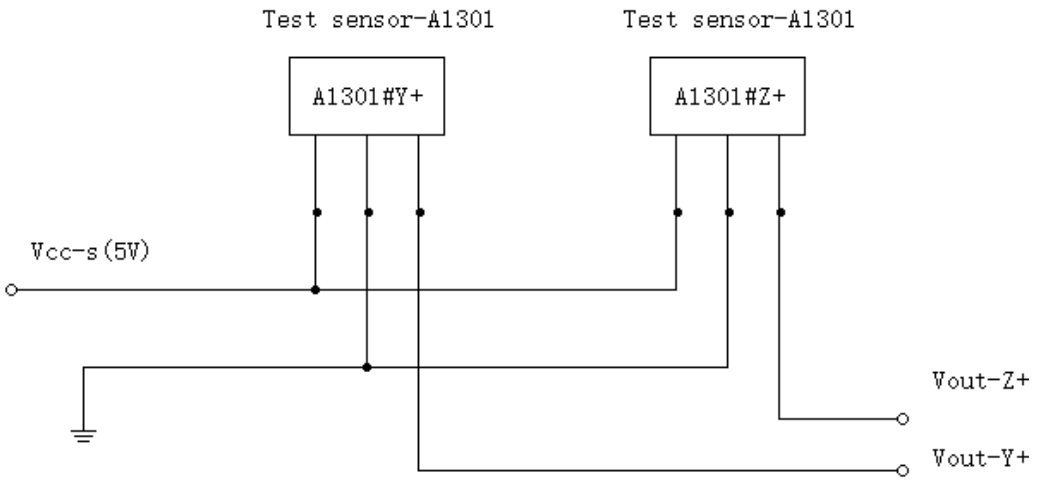

Figure 3.7: Circuit schematic for probe head.

3.3.2 Multi-stage amplifier system

The maximum magnitude of the magnetic field expected is about 0.5 G. Then the magnitude of the Hall Effect sensor output voltage may be on the order of mV. Therefore, an

amplifier is needed to boost the signal to a level significantly above the noise floor and minimum bit size of the A/D converter, in order to achieve maximum signal fidelity. In practice, this means that the A/D converters should be fed a signal on the order of Volts. Therefore, a voltage gain of 10^2 is required. The multi-stage amplifier here also functions as a signal conditioner, i.e. it provides filtering, level-shifting, and buffering, as well as gain.

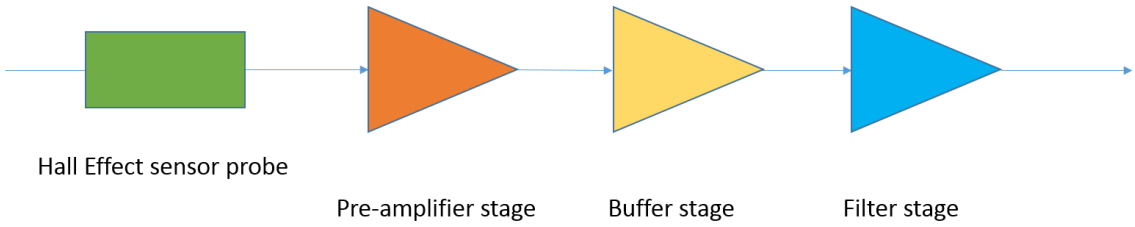

Figure 3.8: Block diagram of the multi-stage amplifier system.

3.3.2.1 Instrumentation amplifier and chip selection

An instrumentation amplifier usually has two inputs and one output [50]. The main function of the instrumentation is to produce an output signal which is proportional to the difference between two inputs in voltages:

$$V_{out} = A_v \cdot \Delta V = A_v \cdot \left(V_{in+} - V_{in-}\right) \tag{3.4}$$

where A_v is the gain of the instrumentation amplifier; V_{in+} and V_{in-} are the input voltages at the noninverting and inverting inputs, respectively.

A monolithic instrumentation amplifier was chosen for this work. The AD620AN is a low cost, high-quality monolithic instrumentation amplifier [51]. The AD620 is designed to offer accurate gains using 0.1% to 1% resistors. Its gain is programmed by a single external resistor R_g , ranging from 1 to 10,000 (Equation (3.5)).

$$A_v = \frac{49.4k\Omega}{R_g} + 1 \tag{3.5}$$

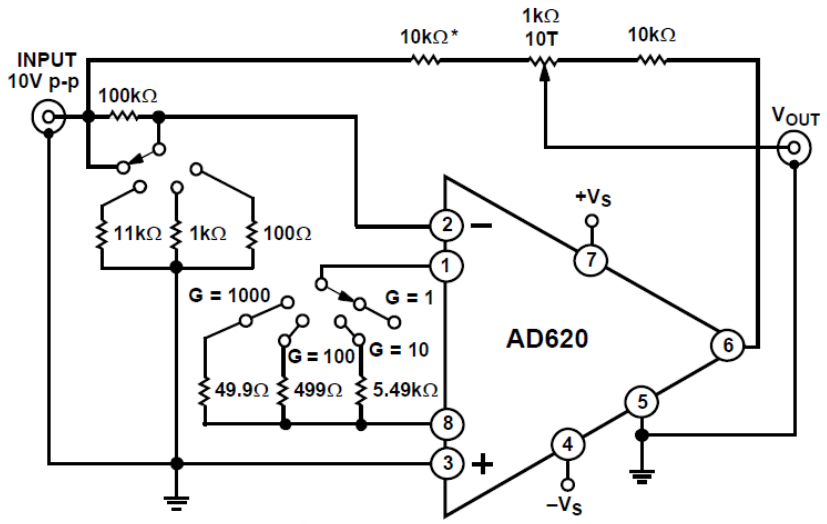

Figure 3.9: Schematic of the AD620A [51].

While an instrumentation amplifier can be made with three or more op-amps, using a monolithic integrated instrumentation amplifier is a smaller-size and low noise option compared with the custom building. It features 8-lead packaging and requires low power which makes it a good fit for our work because dc battery packs were used to power the circuit. The AD620 has 40 ppm (parts per million) maximum nonlinearity. Furthermore, the AD620 has a low offset voltage (50 µV at max), a low offset drift, a high common-mode rejection ratio (100 dB min, when Gain=10) and a low input bias current (2.0 A at maximum). These parameters make the AD620 well suited for this application.

Due to the calculation in [52], the AD620 can work well as a preamplifier because of its low input voltage noise of 9 nV/√Hz at 1 kHz and a 11.5 nV/√Hz total RTI (referred to input) noise when the gain is set to be 10. The RTI noise is 0.28 µV p-p (this corresponds to 112 µG p-p

for this work) in the 0.1 Hz to 10 Hz band where the gain ranges from 100 to 1000. The input current noise is 0.1 pA/√Hz. Also, according to the datasheet [51], the AD620 is well suited for multiplexed applications with its settling time of 15 μs to 0.01%, and its cost is low enough to enable designs with one instrumentation amplifier per channel.

3.3.2.2 Multi-stage amplifier design

A review of the electronic circuit design for each stage of amplification is presented in this section.

Signal source: A1301 Hall Effect sensor measuring circuit

According to the Hall Effect sensor A1301 datasheet [51], the A1301 sensor has a ratiometric output voltage, set by varying the supply voltage from 4.5 V to 6 V [49]. For our case, the supply voltage for the sensors is 5 V.

Currently, the practical power supplies are made with one-chip regulators (7805 regulator). The regulator is a three-terminal chip which takes an unregulated dc input voltage containing ripple and produces a highly regulated dc output voltage with very low ripple [53]. For this work, the L7805 was selected as the regulator chip [54]. For our case, the input voltage Vcc of the 7805 is +9 V. Figure 3.10 shows the correct way to connect to the A1301.

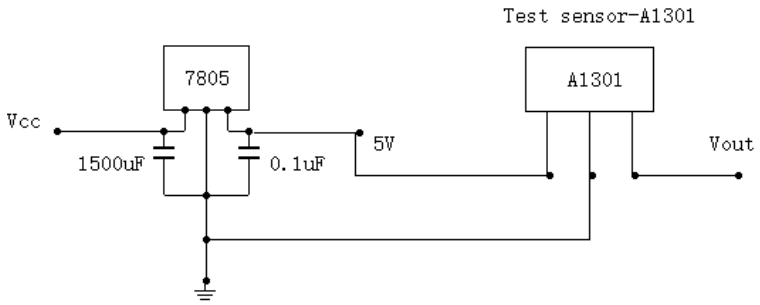

Figure 3.10: Circuit diagram for magnetic sensing circuit based on the A1301 Hall-Effect sensor. The A1301 requires a 5 V supply voltage, in this case, provided by a standard 7805 regulator.

Stage 1 Pre-amplifying

The first stage for the amplifier circuit is to pre-amplify the signal by a definite gain. For the work in this thesis, the theoretical total magnetic field ranges from 0~20 G (based on the results from matlab simulation). Since the sensitivity of the Hall Effect sensor is 2.5 mV/G, the suitable gain should be set around 100 to 1000. After several tests, the external gain resistor was chosen to be 250 Ω. Using Equation (3.5), this corresponds to a gain of 198.6.

An extra Hall Effect sensor was placed to act as a dummy sensor. The output of the dummy sensor becomes the inverting input. Without any applied field, the inverting input voltage of the instrumentation amplifiers is the quiescent voltage of the dummy sensor, monitored by a HP3468A digital multimeter (HP3468A-DVM). At the beginning of every scan, the quiescent voltage value of the dummy sensor (labeled as the pin2#1) was recorded.

Herein this thesis, the pinX#Y denotes the pin X on the chip Y.

The whole circuit design for stage 1 is illustrated as shown in Figure 3.11.

Because the AD620 output voltage was developed with respect to the potential on the reference terminal, many grounding problems may occur in practice. One solution is to tie the AD620 REF pin (pin#5) to the local ground and all the grounds in the completed measurement device must be tied together.

All the chips in this project are supplied by a ±9 V dc battery group. The reason why the battery groups were used is that they can isolate from ac signal noise and other EM interference. Although the battery's 5 hours lifetime is a bit short, the noise reduction and elimination of ground loop problems make this a good choice.

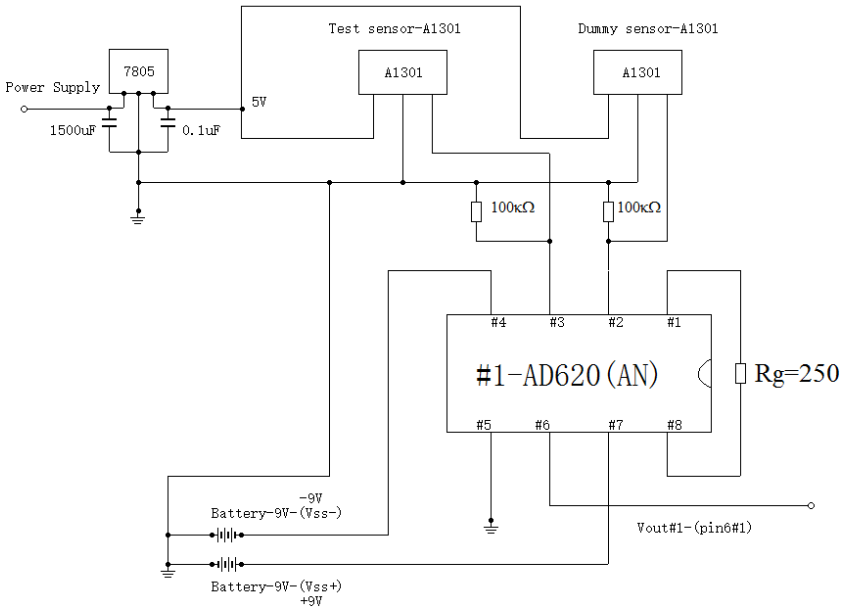

Figure 3.11: Stage 1:Pre-amplifier with a gain of 198.6.

Stage 2 Buffer

After experimentation, a buffer stage is needed following stage 1. (Referred to Section 3.3.4.) The voltage follower can provide impedance conversion from a high level to a low level; essentially it acts as an impedance transformer (or current amplifier).

A voltage follower has a voltage gain very close to unity and a high current gain; in other words, all the output voltage is fed back, which make it useful for interfacing between multiple sensor devices and signal processing devices. Additionally, a voltage follower has high input

impedance (the high input resistance and low input capacitance), low output resistance, and a large bandwidth; thus, changes at the output will have almost no effect on its input and it will draw almost no current from its input.

To avoid the incompatible issue, another AD620A amplifier chip (the same type in stage 1) is used, with voltage gain set = 1.0. Unity gain was obtained according to Equation (3.5), by disconnecting the R_G pins (pin1#2 and pin8#2) which gives $R_G = \infty$. The output voltage of the stage 1 (pin6#1) acts as the non-inverting input of the instrumentation amplifier (pin3#2); and a potentiometer was applied to divide a voltage between +9 V and -9 V. The circuit diagram is shown in Figure 3.12.

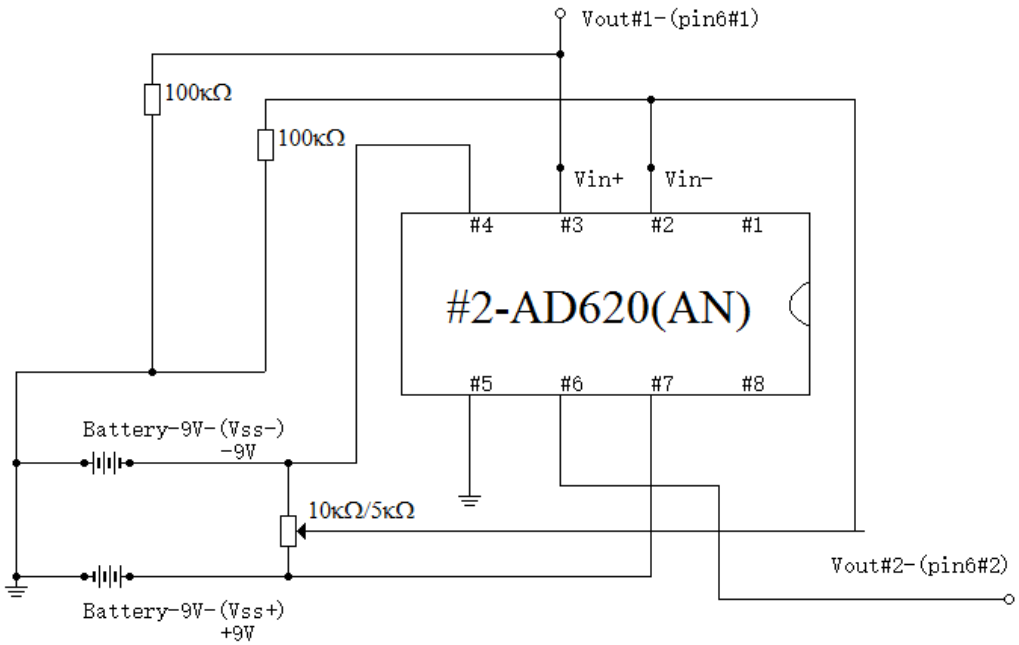

Figure 3.12: Stage 2: voltage follower as a buffer stage.

The analogue-to-digital convertor (ADC) used for the Arduino analogue input is a single-ended 10-bit ADC with a dynamic range from 0 V to +5 V, which means that the minimum analog input value is around 5 mV($\Delta V_{\min} = \frac{5\text{ V}}{1024} \approx 5\text{ mV}$). Therefore, the inverting input at the stage 2 is also used to scale the voltage offset of the final voltage output. (Regarding the Arduino

input voltage, we need to scale the output voltage offset to +2.5 V so as to construct a bipolar magnetic measurement device.) This voltage (pin2#2) should be recorded for the later transformation calculation. The offset of the second instrumentation amplifier (pin2#2) must be set so that we can get a full range.

Stage 3 Signal filtering

A simple low-pass filter is built in stage 3 to filter out high frequency. LM741 type is the general purpose op-amp series, without latch-up when the common mode range is exceeded. An offset nulling circuit is shown in Figure 3.13.

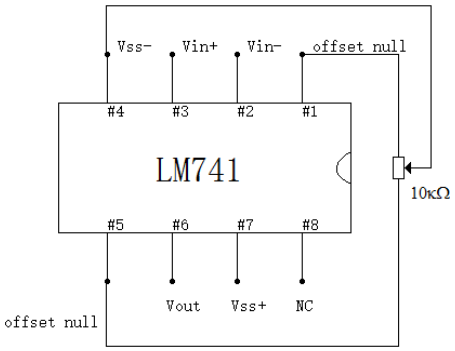

Figure 3.13: Offset nulling circuit for the op-amp LM741.

Because almost all instrumentation amplifiers rectify small out-of-band signals, the disturbance may appear as a small dc voltage offset. High frequency signals then must be filtered with a low-pass active network (See Figure 3.14).

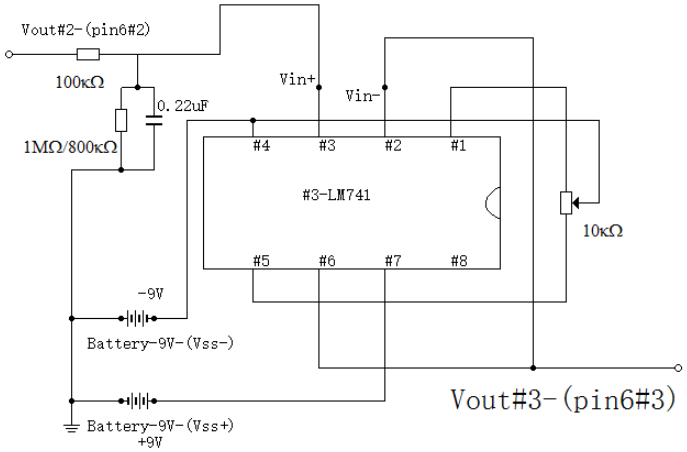

Figure 3.14: Stage 3: Low-pass active filter circuit.

3.3.2.3 Multi-stage amplifier system summary

Figure 3.15 shows the citcuit diagram for the entire multi-stage amplifier system.

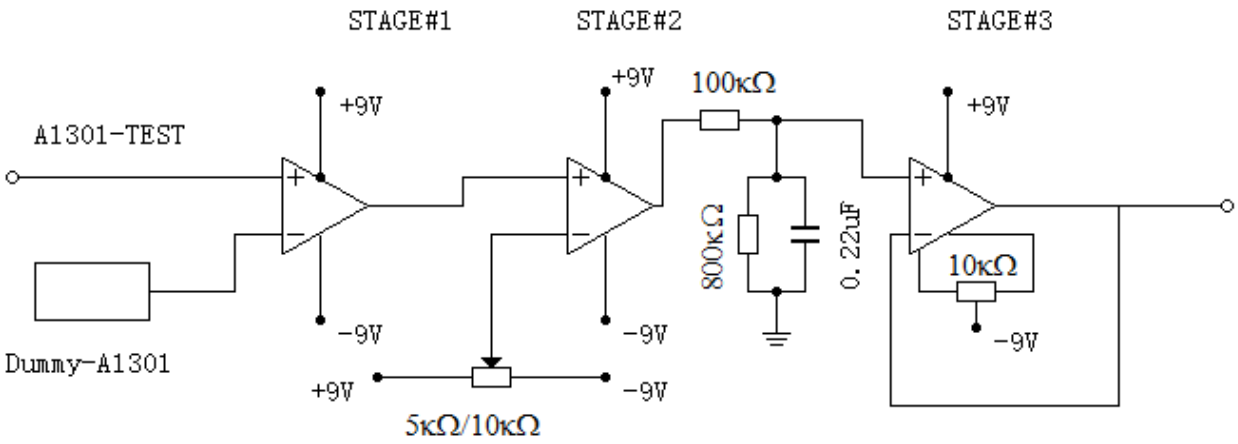

Figure 3.15: The simplified schematics of the amplifier circuit design (one channel).

3.3.3 Movement-systems

The compact MRI Field Mapper (field-mapper) designed and fabricated by an EP495 Physics group [55] was used for the work in this thesis. The field mapper was originally used to map the magnetic field of a wrist-sized LT Imaging Inc. MRI, which uses permanent magnets arranged in a manner similar to a Halbach array. It consists of a 3-axis linear stepper motor

system (SMS)-Shapeoko 2 machine (see Figure 3.16), probe and the data acquisition hardware: Arduino boards with related software. For this work, we used the field mapper with constructed probe and amplifier circuits, to map the magnetic field produced by the RF encoding birdcage current and then to verify the theory.

The field mapper is retrofitted from the Shapeoko2 machine. Shapeoko 2 is a pre-manufactured open source CNC machine, which has been adapted by the EP495 team as the main part of their project [56]. It comes with the Grbl software loaded onto the Arduino. This Grbl software [57] takes G-code inputs and moves the step motor system accordingly. G-code is a programming language, commonly used for computer numerical control (CNC) machines. The Grbl is also an open source alternative to parallel-port-based motion control, mostly used for CNC milling.

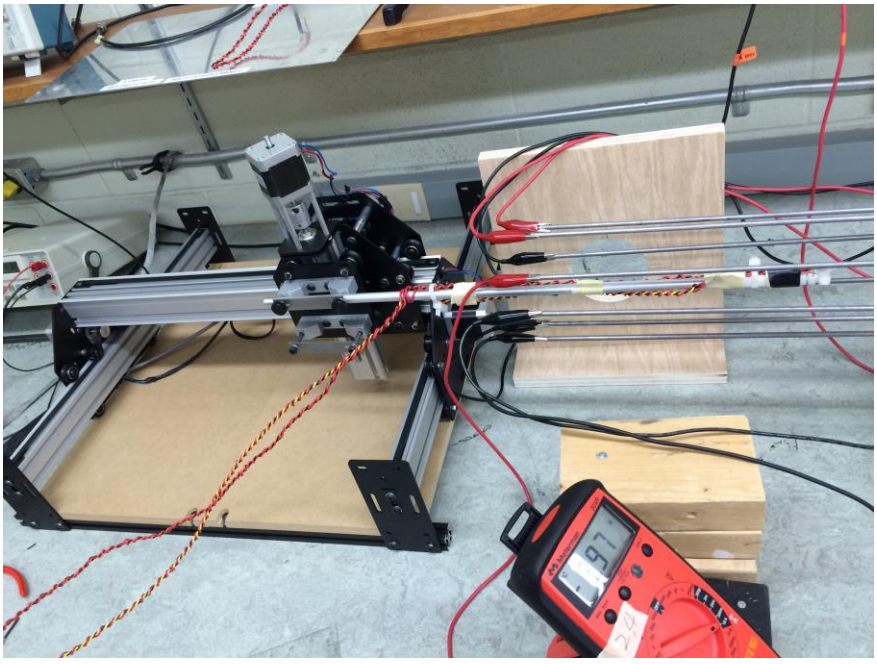

Figure 3.16: Field-mapper movement system. It is designed around the Shapeoko 2.

The EP495 team's work was to replace the Shapeoko 2 router with the probe bar. Since the actual travel in the Z axis can be up to 150 mm (larger than 54mm, the instructed travel length) and its travel was adequate, the field mapper was used in this work as movement system.

In regards to the SMS software, the EP495 team did not write out the G-code commands into an independent text editor but wrote a C program (path_generator.c) that created the G-code. Their C code was generated using a built-in visualization tool. (The C program flow chart can be found in [55].) In the Universal G-code Sender, there is a built-in visualization tool for a given tool path written in G-code. It allows the user to view the tool path in 3D. Thus, using this visualization tool, one can map out the physical shape of the movement path and troubleshoot the C program.

According to the manual of the field mapper [55], the measureable volume is $10\text{cm} \times 10\text{cm} \times 10\text{cm}$ with a less-than-1mm-resolution.

Since the field mapper is relatively inexpensive and it includes all parts needed for the acquisition (discussed in detail later) and movement, this all-customizable approach is the best-fit to our work.

3.3.4 Data acquisition

The DAQ component of the field mapper was chosen to use. In field mapper, there are two Arduino UNO microcontroller boards: one is for motion control of the Shapeoko2 machine, the other is for the data acquisition. The EP495 team wrote a sketch program (analoginputloop.file), then compiled and uploaded it to the Arduino.

The main function of the program is to read the voltage values from the analog input pins on the Arduino boards; convert them into the magnetic field values (Unit: Gauss); then send to the file to be recorded. The Arduino board has a built in analog-to-digital conversion program from which the code can be easily modified for our experiment. This can be considered in the post-processing part. More details about the Arduino [58] and the code may be found in the EP495 team report [55].

The following three points are important for the system design:

1. In the field mapper system, five out of the six analog input pins on the Arduino board are used.

2. In the programming code, the Arduino averages the reading of two pins. For example, the B_{y+} B_{y-} denote the magnetic field value at the left and right sensor respectively, then the returned B value in the y axis should be as obtained by :

$$B_y = \frac{1}{2}\left(B_{y+} - B_{y-}\right) \tag{3.6}$$

3. The analog inputs on the Arduino are 10-bit A/D converters, which means that the reading from the analog inputs ranges from 0 to $2^{10} - 1 = 1023$. Since the voltage supply of the Arduino is 5 V, 0 corresponds to a voltage of 0 V and 1023 corresponds to a voltage of +5 V.

The Hall Effect sensor are offset so that the output voltage is +2.5 V when there is no magnetic field. This means that the magnetic field passing through the sensor in the positive direction gives the output voltage above +2.5 V; the B field passing through in the negative direction gives the output voltage below +2.5 V.

This can also explain why a buffer stage in the amplifying design was inserted: to adjust the offset voltage. (See the Section 3.3.2) The converting equation from the analog pins to the magnetic field is given by :

$$B = \frac{\frac{5\text{V}}{1023} - 2.5\text{V}}{0.0025\text{V/G}} \tag{3.7}$$

The EP495 team wrote a python script (fieldmapper.py) for ease of use. The python code asks the users for several inputs regarding the initial setup and the scan parameters such as the radius of the scan, the length of the cylinder, desired step-size and so on. Meanwhile, it can also create a text file for storing the data. The flow chart for the software of the field mapper and the programming code in detail may be found in [55] .

3.3.5 Post-processing

In summary, the field mapper uses the C program (path_generator.c) and the users' input (from the fieldmapper.py) information to generate the desired tool path for the probe. Then the Arduino code (analoginputloop.file) reads the analog input values from each Hall Effect sensors, and converts them in Gauss. According to the python code, the data is sent into a new-created text file. This file contains the probe position information as well as the B field value at the position.

The field mapper movement part and the DAQ part are used for this work. Therefore the data obtained from the field mapper's text data file is not as expected. A transformative calculation should be made before plotting.

The transfer function for both channels are:

$$B_{CHNY+}(Gauss) = 400 \times \left(pin2\#1 - pin3\#1(t=0) + \frac{\frac{1023}{1000} \times B_Y(rawdata) + pin2\#2}{Avy} \right)$$

(3.8)

$$B_{CHNZ+}(Gauss) = 400 \times \left(pin2\#1 - pin3\#1(t=0) + \frac{\frac{1023}{1000} \times B_Z(rawdata) + pin2\#2}{Avz} \right)$$

(3.9)

Upon inspection of Equations (3.8) and (3.9), it can be seen that the undetermined coefficients are $pin2\#1$, $pin3\#1(t=0)$ and $pin2\#2$, which represent respectively the dummy sensor output voltage, the testing sensor output sensor before sensing (i.e. the quiescent output voltage) and the amplifier offset voltage. The values (i.e. 400, 1023, and 1000) were determined by a separate calibration step.

CHAPTER 4

EXPERIMENTAL RESULTS AND ANALYSIS

4.1 Measurement device design calibration

In the previous sections, the measurement device design was described. Among them, a key component is the amplifier part. In this section, a few calibration tests were described which verified that the amplifier-design and the measurement device worked well.

Experiment 1 was to test the AD620A chip performance;

Experiments 2 to 5 tested the performance of the Stage 1 circuit (pre-amplifying stage) by comparing with the Gauss meter reading;

Experiments 4 and 5 verified whether the measurement results obey the Biot-Savart law;

Experiments 6 and 7 tested the performance of the complete amplifier circuit design, as well as to find the experimental gain and the offset voltage for both channels (Y+, Z+).

The Table 4.1 lists a summary of the plots and the linear regression equation information from the calibration tests. Among the experimental results, there are two values should be noticed: the experimental gain value for the Y+ and Z+ channels, in that they are needed in the post-processing stage for the later experiments.

TABLE: SUMMARY OF MAGNETIC FIELD CALIBRATION TESTS								
Test Experiment Number#	Best-Fit Slope	Best-fit y-intercept	Correclation coefficient-Pearson'R	x	x-unit	y	y-unit	Comments
1	4.9780	0.0105	0.9984	Differencial voltage=(pin3)-(pin2)	[Volts]	Vout(pin6)	[Volts]	**DC Gain Characterization plot of AD620 chip using in Stage 1 of the circuit**
2	0.6217	0.9708	0.9998	I_magnetic	[mA]	B field	[Gauss]	**B field vs I magnet(the B field is measured by F.WBell Gauss Meter)**
2	-2.5477	2.5295	0.9998	B field by Gauss Meter	[Gauss]	dV at Pin3#1	[mV]	**A1301Testbar Hall effect sensor voltage output changes dV vs B field**
2	-0.7433	1.5952	0.9983	B field by Gauss Meter	[Gauss]	Output Voltage(pin6#1)	[Volts]	**Output Volatge (Stage 1) vs B field(Gain=198.6 Vcc=±9V Battery)**
2	278.42	0.7663	0.9591	Vinput=(pin3#1-pin2#1)	[Volts]	Vout(pin6#1)	[Volts]	**dc Gain Characterization of Amplifier Stage 1(Gain=198.6 Vcc=±9VBattery)**
3	0.5855	0.7291	0.9984	I magnet	[mA]	B field measured by FW Bell 4048	[Gauss]	**I magnet vs B field**
3	-0.7051	6.9737	0.9836	B Field	[Gauss]	Output voltage(pin6#1)	[Volts]	**Output Voltage (Stage 1) vs B field within 2Gauss**
3	-0.7006	7.0057	0.9838	B Field measured by FW BELL 4048	[Gauss]	Output voltage(pin6#1)	[Volts]	**Output Voltage (Stage 1) vs B field within 2Gauss (the voltage is measured by FW BELL 4048)**
3	271.56	1.4719	0.9888	Vinput=(pin3#1-pin2#1) measured by FW BELL 4048	[Volts]	Vout(pin6#1)-DVM	[Volts]	**dc Gain Characterization of Amplifier Stage 1-measured by FW BELL 4048**
3	273.35	1.4034	0.9887	Vinput=(pin3#1-pin2#1)	[Volts]	Vout(pin6#1)	[Volts]	**dc Gain Characterization of Amplifier Stage 1**
6	-0.5858	-0.4102	0.9990	I_magnet	[Ampere]	B field	[Gauss]	**Channel 1:B field vs I_magnet-Case1=pin2#2=-0.81864**
6	-0.5843	-0.3432	0.9989	I_magnet	[Ampere]	B field	[Gauss]	**Channel 1:B field vs I_magnet-Case2=pin2#2=-0.99518**
6	-0.5834	-0.3744	0.9986	I_magnet	[Ampere]	B field	[Gauss]	**Channel 1:B field vs I_magnet-Case3=pin2#2=6.0155**
6	-0.5795	-0.1877	0.9987	I_magnet	[Ampere]	B field	[Gauss]	**Channel 1:B field vs I_magnet-Case4=pin2#2=-2.86704**
6	-0.5774	-0.1743	0.9986	I_magnet	[Ampere]	B field	[Gauss]	**Channel 1:B field vs I_magnet-Case5=pin2#2=3.4422**
7	-0.6014	-0.5580	0.9989	I_magnet	[Ampere]	B field	[Gauss]	**Channel 2:B field vs I_magnet-Case1=pin2#2=-2.01952**
7	-0.5981	-0.5447	0.9990	I_magnet	[Ampere]	B field	[Gauss]	**Channel 2:B field vs I_magnet-Case2=pin2#2=0.28098**
7	0.5241	0.2050	0.9992	Output Voltage-DVM (pin6#2)[Volts]	[Gauss]	Output voltage(pin6#1)	[Volts]	**Channel 2:Output Voltage-DVM vs B field -Case2=pin2#2=0.28098**

Table 4.1: A summary of the plots and the linear regression information of the calibration tests. Experiment 1 tested the AD620A chip performance. Experiments 2 to 5 tested the performance of the Stage 1 circuit (pre-amplifying stage) by comparing with the Gauss meter reading; Experiments 4 and 5 verified whether the measurement results obey the Biot-Savart law. Experiments 6 and 7 tested the performance of the complete amplifier circuit design, as well as to find the experimental gain value and the offset voltage for the both channels(Y+, Z+).

4.2 Eight-DC-bar experiments

The amplifier channels have been discussed in the previous section. Figure 4.1 shows the complete experimental system, which is used to perform the experiment described in the thesis. It is important to note that herein two Arduino boards are used. One is for motion control, the other is for the data acquisition.

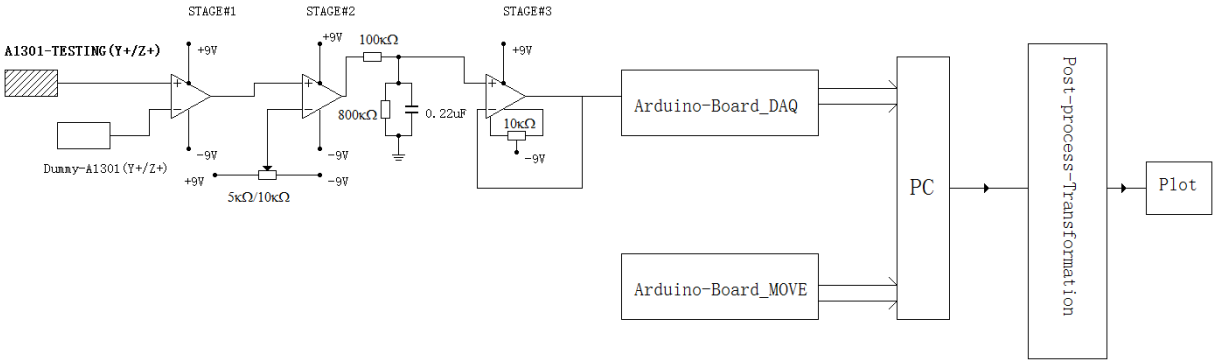

Figure 4.1: Overview of the experiment measurement for one channel.

4.2.1 Experimental method

4.2.1.1 Hardware configuration: Arduino board connection

Since the amplifier circuit outputs an analog signal, the signal needs to pass through an Analog to Digital (A/D) converter, which is done by an Ardunio board. Another Arduino board is included in the fieldmapper for the three-axis stepper motor control.

The Arduino boards take care of fieldmapper control and the interface with the probe sensors. However, only one Arduino board is active. Thus, when the Arduino-DAQ is working, the fieldmapper is completely still; when the Arduino-Move is working, the probe is not taking any measurements. There are six pins for the analog input on the Arduino board, but for our use,

five pins were used, based on the fieldmapper software program code. Therefore, the connections were as shown as in Table 4.2.

Pin number	Connection
0	GND
1	Z+ channel pin6#3
2	GND
3	Y+ channel pin6#3
4	GND

Table 4.2: Arduino board connection.

4.2.1.2 Software configuration: Python processing condition

After the fieldmapper is positioned properly and both Arduino boards are connected correctly to the computer, the scans start by running the python software. As the previous chapter introduces, a python script is responsible for running the mapper. Then the data acquisition begins and a timer starts. After the data run is complete, a text file recording the data is created. This data is called raw data.

When running the python program, there are a series of commands that prompt the user for inputs at the beginning which are listed in Table 4.3. Note that the radius of the scanning area (R_scan) for one slice is calculated by :

$$R\_scan = Radius - \frac{Diameter}{2} \tag{4.1}$$

where the $Diameter$ is the inputs of the magnetic field probe-head size.

Inputs	Definition
Unit	The units the user wish to use: millimeters (mm) or inches
Radius	The radius of the cylindrical volume to be mapped
Length	The total length of the cylindrical volume
Slice	The number of the slices over the length to be mapped
Stepsize	The spatial step-size betwenen each measurement
Diameter	The magnetic field probe-head size

Table 4.3: The inputs required by the python program.

A detailed summary of the processing conditions for each group is given in Table 4.4. Therefore, the scan radius for one slice equals to 25mm.

The python program also asks the user to type in the name of the data file. For this work, the naming rule is as 'Case[X]_[Y]_[Z]', where [X]=1, 2, 3 represents case $Ga = \pi, 2\pi, 3\pi$; [Y]=1, 1.5, 2, 2.5, 3, 3.5, etc. represents the index value (scaling factor); [Z]=1, 2, 3, etc. represents the group number.

Inputs	Value
Unit	millimeters
Radius	40mm
Length	1mm
Slice	1
Stepsize	1mm
Diameter	30mm

Table 4.4: Summary of the conditions for the scanning

4.2.1.3 Post-processing the raw data

The raw data need to be post-processed before plotting as mentioned in Section 3.3.5. According to the results of the dc gain characterization for the two channels (see summary of the

calibration tests plots in Table 4.1), the experimental gain value for two amplifier channels was determined.

Taking the gain value and the other initial conditional variable value into Equations (3.8) and (3.9), the experimental magnetic field for the both channels in Gauss (B_{CHNY+} , B_{CHNZ+}) can be obtained.

The amplitude and the phase of the magnetic field are :

Amplitude $$B(y,z) = \sqrt{B_{CHNY+}{}^2 + B_{CHNZ+}{}^2} \tag{4.2}$$

Phase $$\theta(y,z) = \arctan(\frac{B_{CHNZ+}}{B_{CHNY+}}) \tag{4.3}$$

With the corresponding position information, the results were plotted using Matlab software [37]–[41], [53] (Herein, the raw data file was imported into an excel datasheet; then the transformation was carried out within the excel file)

4.2.1.4 Ampère's law test

In order to test the performance of field mapping apparatus shown in Figure 4.1, the device was tested with a single bar current ($I = 10.09$ A was given onto the top bar of the birdcage coil, see Figure 4.2) to see if the constructed magnetic field measurement tool gave correct results. The answer is positive if the measurements obey Ampère's Law.

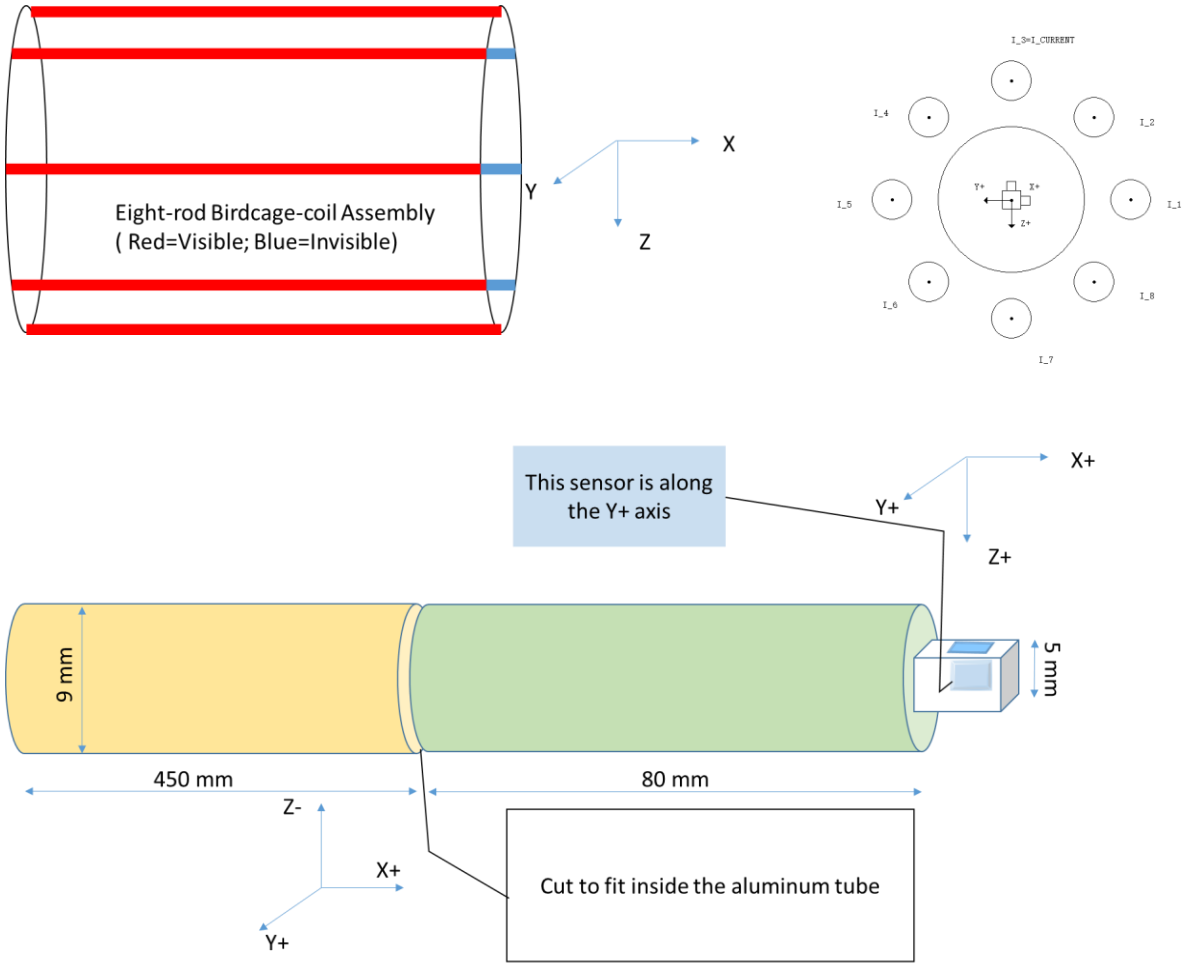

Figure 4.2: Diagram of the birdcage coil assembly used in the experiment. This assembly can also be used to test Ampère's Law.

4.2.2 Current scaling factor

Recall the RF encoding birdcage-coil current from Chapter 2: for each case, the current value applied on each aluminum rod is shown in Table 4.5 and Figure 4.2. (Unit: Ampere (A), except notice.)

	$Ga = \pi$		$Ga = 2\pi$		$Ga = 3\pi$	
	Calculation	Theoretical	Calculation	Theoretical	Calculation	Theoretical
i_1	-0.699	-0.70	-0.944	-0.94	-0.567	-0.57
i_2	0.384	0.38	-0.989	-0.99	-3.951	-3.95
i_3	2.159	2.16	4.597	4.60	9.76	9.76
i_4	0.384	0.38	-0.989	-0.99	-3.951	-3.95
i_5	-0.699	-0.70	-0.944	-0.94	-0.567	-0.57
i_6	-0.544	-0.54	-0.265	-0.27	-0.039	-0.04
i_7	-0.441	-0.44	-0.164	-0.16	-0.023	-0.02
i_8	-0.544	-0.54	-0.265	-0.27	-0.039	-0.04

Table 4.5: RF encoding Birdcage-Coil leg currents in theory. The calculation here represents the calculations given in Section 2.4; the theoretical here represents the values in theory which are used in the later experiments.

In order to increase the resulting field, the current on each leg was multiplied with an index (herein it is called scaling index). The reason for this is to boost the acquired signal above the noise.

Limited by the maximum value of the current power supply in lab (one can output 25 A at maximum, one can output 10 A at maximum and another three can output 3 A at maximum), the experimental current could not be above 10 Ampere. Then, combined with the theoretical value of the leg currents (Table 4.5), the maximum magnetic field in these three cases is simulated to be around 19 G.

A number of experiments were done (ten scans as one group, at least three groups for each trial test) to find appropriate scaling factors, to ensure that the magnetic fields produced by the birdcage coil assembly fell within the dynamic range of our magnetic field measurement system. We finally decide to take the scale factor value as $\times 3.5$, $\times 3.0$, $\times 1.5$ for the case $Ga = \pi, 2\pi, 3\pi$, respectively, which are summarized in Table 4.6.

4.3 Experiment results

Inspection of the results from the scale factor selection experiments (discussed earlier), the best-fit scale factor value and the coil leg currents are tabulated in Table 4.6. With the measurement device described in Chapter 3, the magnetic field generated by the RF encoding birdcage coil within the scanning area was then mapped.

	$Ga = \pi$			$Ga = 2\pi$			$Ga = 3\pi$		
	Theoretical	scale=3.5	Experimental	Theoretical	scale=3.0	Experimental	Theoretical	scale=1.5	Experimental
i_1	-0.70	-2.45	-2.45	-0.94	-2.82	-2.82	-0.57	-0.86	-0.86
i_2	0.38	1.33	1.35	-0.99	-2.97	-2.97	-3.95	-5.93	-5.93
i_3	2.16	7.56	7.65	4.60	13.80	13.91	9.76	14.64	14.61
i_4	0.38	1.33	1.35	-0.99	-2.97	-2.97	-3.95	-5.93	-5.93
i_5	-0.70	-2.45	-2.45	-0.94	-2.82	-2.82	-0.57	-0.86	-0.86
i_6	-0.54	-1.89	-1.89	-0.27	-0.81	-0.81	-0.04	-0.06	-0.06
i_7	-0.44	-1.54	-1.54	-0.16	-0.48	-0.48	-0.02	-0.03	-0.03
i_8	-0.54	-1.89	-1.89	-0.27	-0.81	-0.81	-0.04	-0.06	-0.06

Table 4.6: RF encoding birdcage-coil currents under different phase gradients. The best-fit results for scale factor selection for the three cases are shown. The calculation here represents the calculations given in Section 2.4; the theoretical here represents the results after rounding the calculations to the nearest hundredth.

The amplitude and the phase contour plots are shown in Figure 4.3. These results are based on the average of the 10 consecutive measurements in each cases. The theoretical magnetic field maps are shown in Figure 4.4.

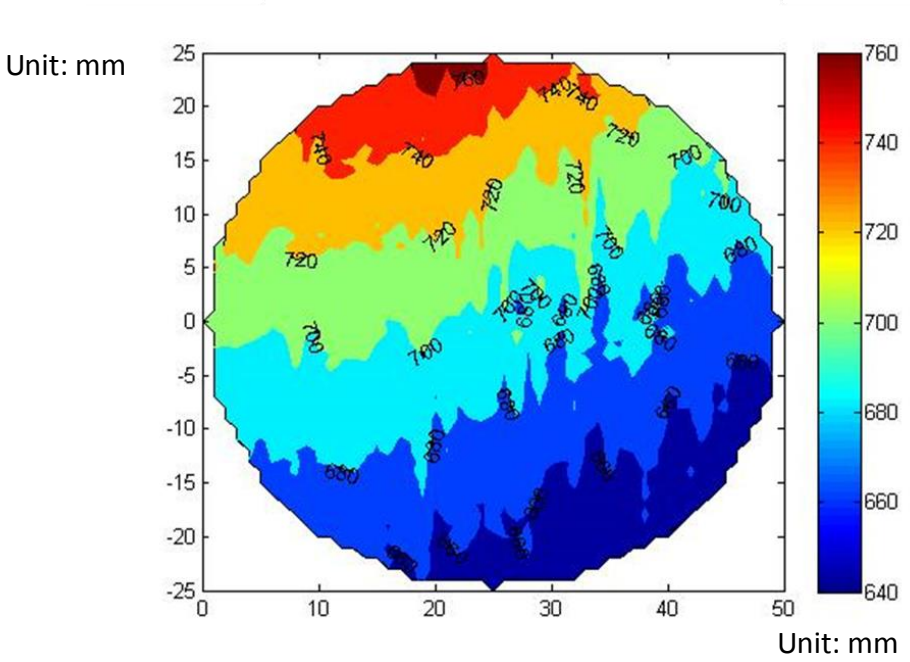

(a) Amplitude map for the $Ga = \pi$ case (Unit: Gauss)

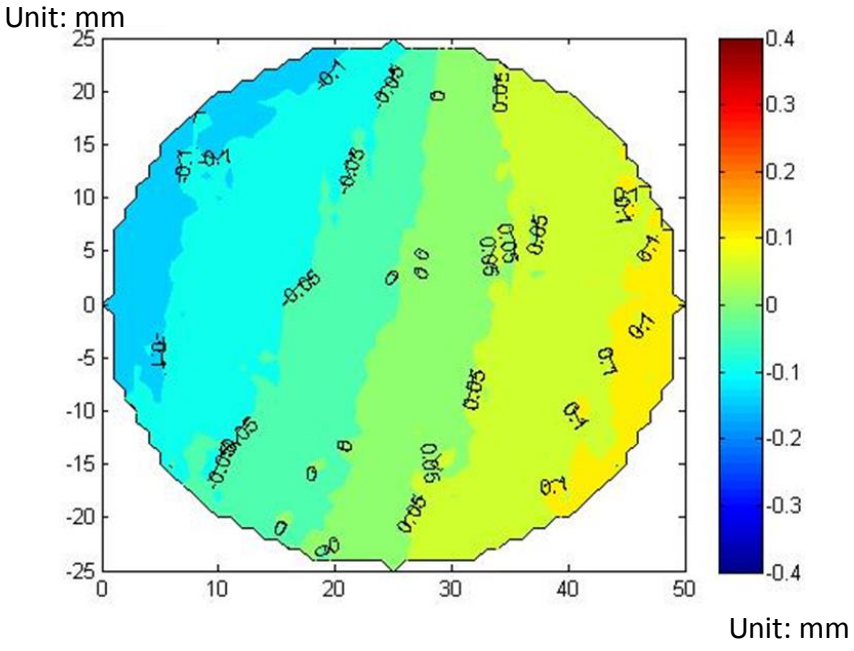

(b) Phase map for the $Ga = \pi$ case (Unit:1)

Unit: mm

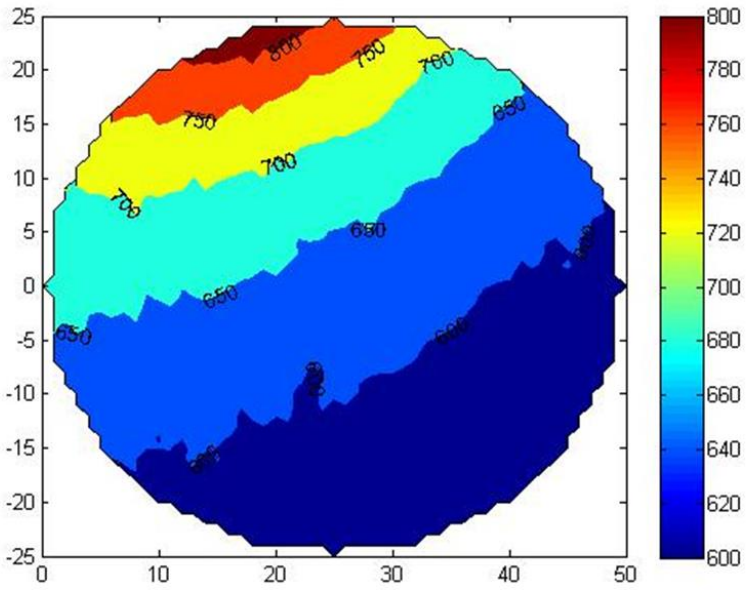

Unit: mm

(c) Amplitude map for the $Ga = 2\pi$ case (Unit: Gauss)

Unit: mm

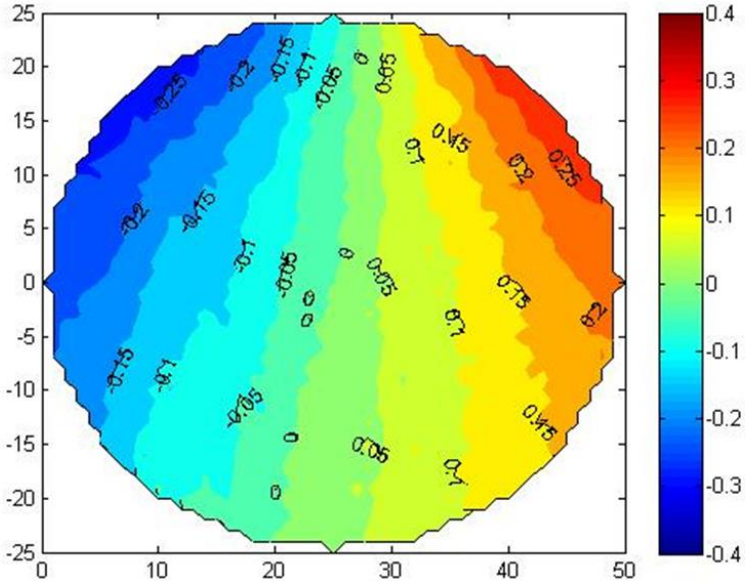

Unit: mm

(d) Phase map for the $Ga = 2\pi$ case (Unit:1)

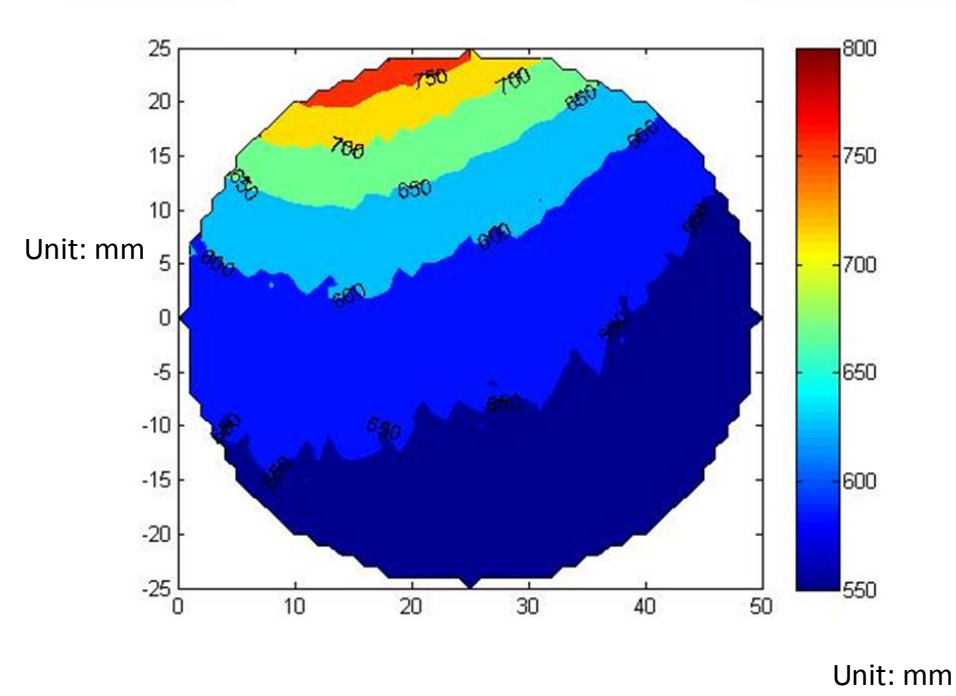

(e) Amplitude map for the $Ga = 3\pi$ case (Unit: Gauss)

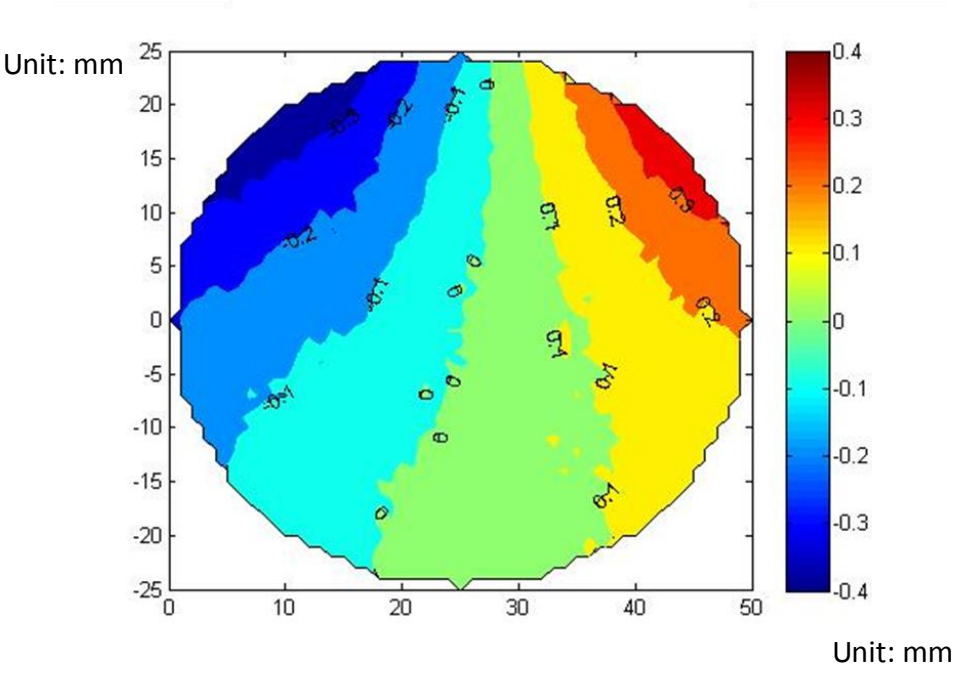

(f) Phase map for the $Ga = 3\pi$ case (Unit:1)

Figure 4.3: Results of the magnetic field map produced by the scaled RF encoding birdcage-coil currents. Unit: Gauss in (a)(c)(e); Unit: 1 in (b)(d)(f).

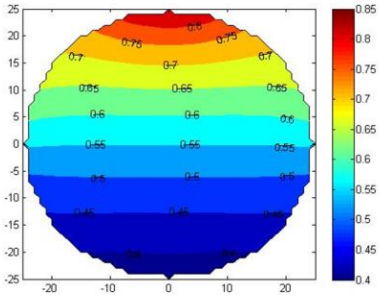

(a) Amplitude map for the $Ga = \pi$ case

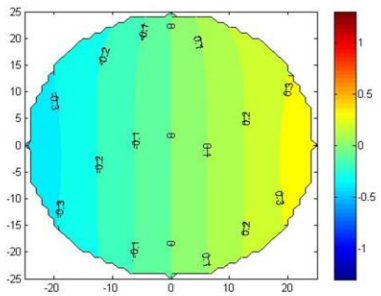

(b) Phase map for the $Ga = \pi$ case

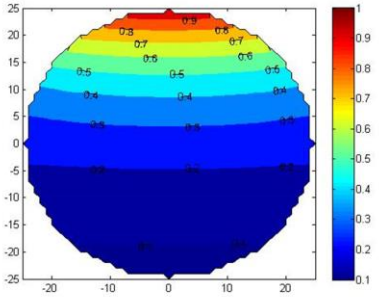

(c) Amplitude map for the $Ga = 2\pi$ case

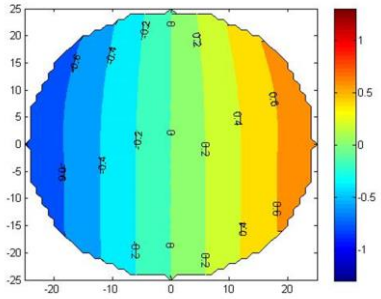

(d) Phase map for the $Ga = 2\pi$ case

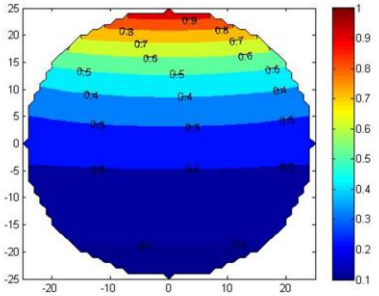

(e) Amplitude map for the $Ga = 3\pi$ case

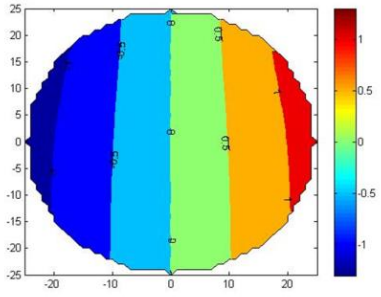

(f) Phase map for the $Ga = 3\pi$ case

Figure 4.4: Simulation results of the magnetic field map produced by the scaled RF encoding birdcage-coil currents.

4.4 Discussion

It could be observed that the amplitude maps in Figure 4.3 and 4.4 that the experimental values agree with the theory roughly even though there is a tilt. However, in this thesis work, the phase information is more concerned than the amplitude information of the total magnetic field. Merging the phase plots in the Figure 4.3 and 4.4 into one figure, the Figure 4.5 below shows the phase information in the theory and as measured for each cases.

From the results in Figure 4.5, it can be observed that the minimum and maximum phases for the case $Ga = \pi$ are $\theta\min = -0.1554$ and $\theta\max = 0.1415$; then the phase difference is $\Delta\theta_{case1} = 0.2969$. For the case $Ga = 2\pi$, $\theta\min = -0.3010$ and $\theta\max = 0.2930$; then the phase difference is $\Delta\theta_{case2} = 0.5940$. For the case $Ga = 3\pi$, $\theta\min = -0.3862$ and $\theta\max = 0.3983$; then the phase difference is $\Delta\theta_{case3} = 0.7845$. (These are summarized in the Table 4.7.)

	case 1	case 2	case 3
phase-min	-0.1554	-0.3010	-0.3862
phase-max	0.1415	0.2930	0.3983
phase-difference	0.2969	0.5940	0.7845
relative ratio with case1	1.0000	2.0007	2.6423
theory ratio	1.0000	2.0000	3.0000

Table 4.7: Summary of the phase measurements. Case 1, 2, 3 represent $Ga = \pi$, $Ga = 2\pi$, $Ga = 3\pi$, respectively.

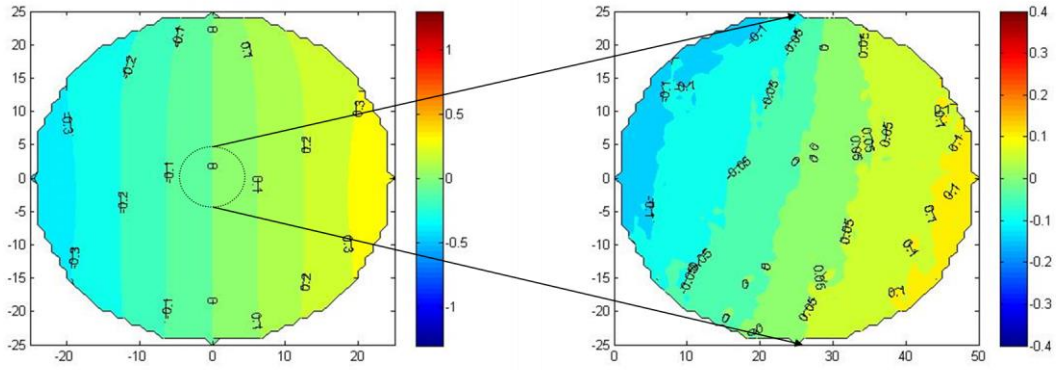

(a)Theoretical: $Ga = \pi$ case (d)Experimental: $Ga = \pi$ case-Note Zoomed in

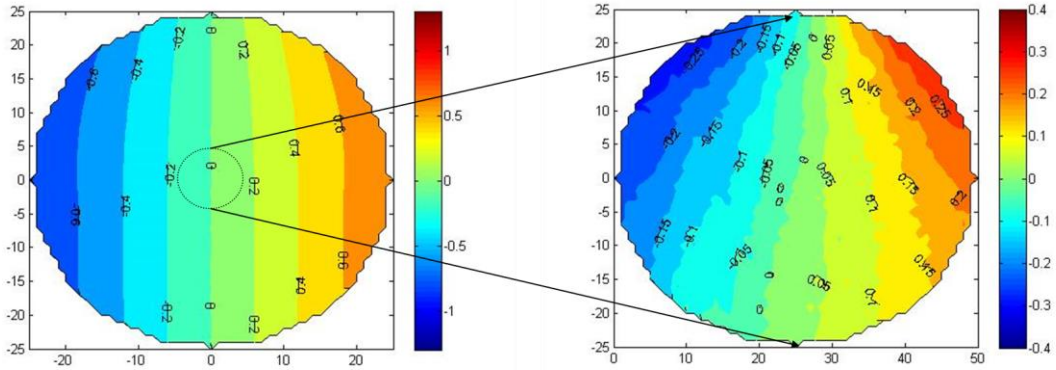

(b)Theoretical: $Ga = 2\pi$ case (e) Experimental: $Ga = 2\pi$ case-Note Zoomed in

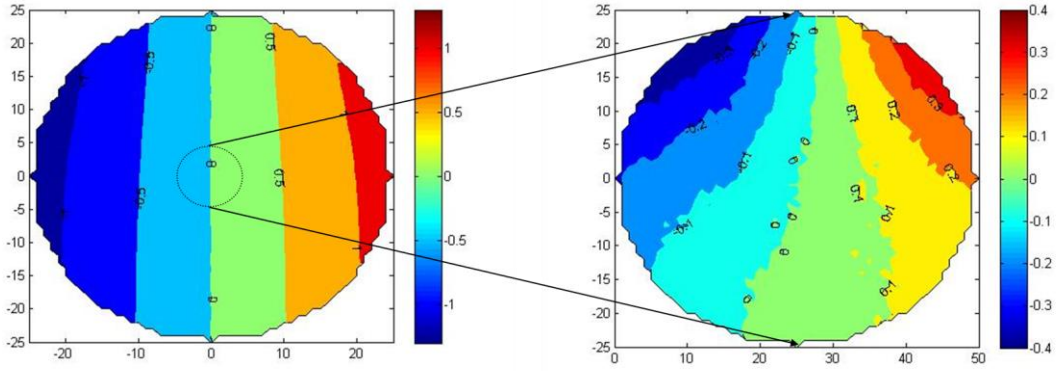

(c)Theoretical: $Ga = 3\pi$ case (f) Experimental: $Ga = 3\pi$ case-Note Zoomed in

Figure 4.5: Results of the phase information of the RF encoding Birdcage-coil. (a)-(c) show the phase maps in theory; (d)-(f) show the experimental measurements of the phase. Unit: 1. Note that the (a)(b)(c) are in the same scale; the (d)(e)(f) are in the same scale. Note that the experimental plots cover the central region of the theoretical plots (indicated schematically on the figures). The scale factor is different for each case.

In summary, based on Figure 4.5 and Table 4.7, the data agrees with the theory. Again, note that the experimental maps (Figure 4.5 (d) & (e) & (f)) are based on the b-circle area of the theoretical field for each cases.

It is found worth noticing that there are some deviations in the phase information between theory and experiment. This may result from the overall twist that the cage setup had with respect to the probe head. Possible reasons are listed as below:

1. The misalignment of the probe axes with the cage setup axes may be the major reason, because the coil cage and the probe are not pinned onto the table.

Inspection of the experimental plots shows a twist angle of about 20 degrees, especially when the phase gradient is large. (It is obvious in the case $Ga = 3\pi$.) Regarding this issue, ten groups were added within a week. The results showed that this 20 degree tilt in the phase figure still existed. By rotating the probe-head around by 15 degrees, it was found that the results became better with less tilt (but still exists) in the phase map.

2. The data of the experiment was corrected by subtracting the effect of the Earth field for the experiment location. However, no obvious difference was visible after the Earth field correction.

Because the expected magnetic field is too small, the Earth field (0.25~0.60 Gauss, the Earth's magnetic field at its surfaces) should be taken into consideration. Like any other magnetic field, the magnetic field of the Earth (B_{earth}) is a vector field, which means that it has a magnitude and a direction [59].

The simplest description of the Earth field is a magnetic dipole (a bit like a bar magnet), but the problem is complicated by the fact that the axis of the dipole and the axis of the Earth are not aligned. In addition there are higher-order multipole moments. As well, the magnetic dipole

wanders a bit over time (although the timescales for this are longish, like tens of years, so this effect will not matter).

Anyway, the important thing is that the magnetic field of the Earth is a vector which is not aligned with the axis of our MRI cage setup. Therefore we need to know orientation of the Earth's magnetic field vector B_{earth} with respect to our MRI cage setup axes first, as well as the magnitude of the B_{earth}.

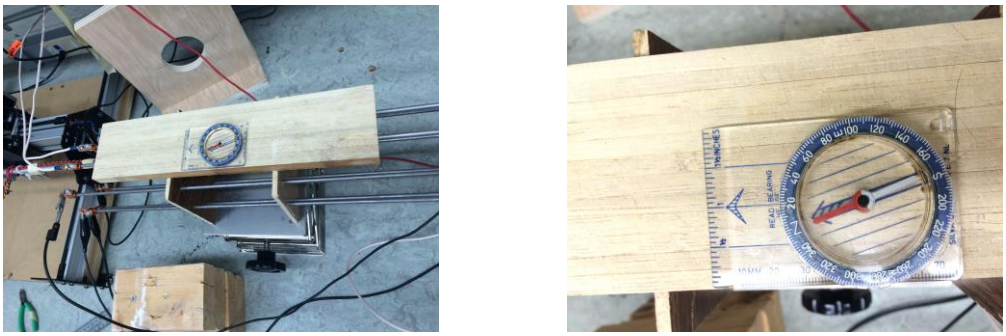

Figure 4.6: Pictures of the measurement of the orientation the Earth field vector with regards to the MRI cage setup axes.

The Earth field vector amplitude has been studied for a long time. Therefore, luckily for this work, the problem has been mostly solved for us. The US National Oceanic and Atmospheric Administration (NOAA) maintains the very nice website [60], which gives the local magnetic declination (declination = angular difference between the True North pole and the Magnetic North pole) and inclination (= "dip angle", measured positive below the horizontal plane) for any location and date (they even have Saskatoon in their database). It also provides the strength of the magnetic field in nT (10 micro Gauss, $1\,nT = 10^{-5}\ G = 0.01\,mG = 10\ \mu G$). The google maps can help to acquaint with geographic location information of the lab. See Figure 4.7.

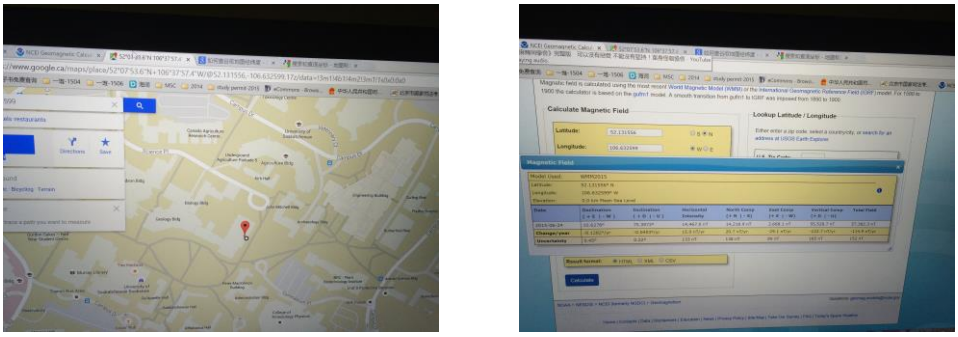

(a) (b)

Figure 4.7: The Earth magnetic field strength by using the Earth field calculator. (a) Google map to locate the geographic information of the lab. (b) Earth field calculator results by the NOAA magnetic field calculator.

Then, using the Earth field calculation (the website [60]), we can get our lab local magnetic field components. After figuring out the projection of these components onto the X,Y,Z axes of our MRI cage, we can subtract the B_X, B_Y, B_Z values for the Earth's field from the data to see whether the shape of the scans can be corrected.

As can be seen in Figure 4.6 and Figure 4.7, the orientation of the cage's long axis with respect to the horizontal component of B_{earth} is measured to be 22 degrees anticlockwise from the axis of the cage assembly, using the compass. The strength of the Earth's magnetic field is $B_{earth} = 0.57367\ G$; the horizontal and the inclination degree are $\theta_{earth}(Horizontal) = 18^{\circ}$, $\theta_{earth}(Inclination) = 75.3968^{\circ}$; the horizontal component is $B_{earth}(Horizontal) = 0.144636\ G$; thus, for our cage setup, the Y+ component and the Z+ component are $B_{earth}(Y+) = 0.044695\ G$, $B_{earth}(Z+) = 0.55514\ G$ respectively. Record these values into the post-processing excel file and correct the data. Then the new phase figures for each cases can be obtained.

The Earth field correction approach 1 is to subtract the Earth field components on each axis; the approach 2 is to plus the Earth field components in each axis. (See Equations (4.4) and (4.5).)

$$\begin{cases} B(Y+)_{after} = B(Y+)_{before} - B_{earth}(Y+) \\ B(Z+)_{after} = B(Z+)_{before} - B_{earth}(Z+) \end{cases} \tag{4.4}$$

$$\begin{cases} B(Y+)_{after} = B(Y+)_{before} + B_{earth}(Y+) \\ B(Z+)_{after} = B(Z+)_{before} + B_{earth}(Z+) \end{cases} \tag{4.5}$$

From the results of the Earth field correction, the tilt in the phase still exists, and it shows that there is little difference between the cases before and after the correction.

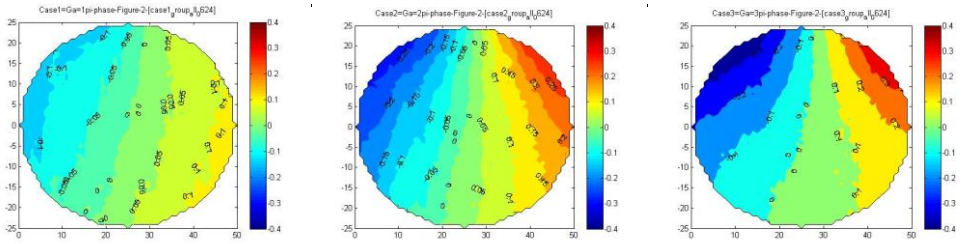

Before the Earth field consideration.

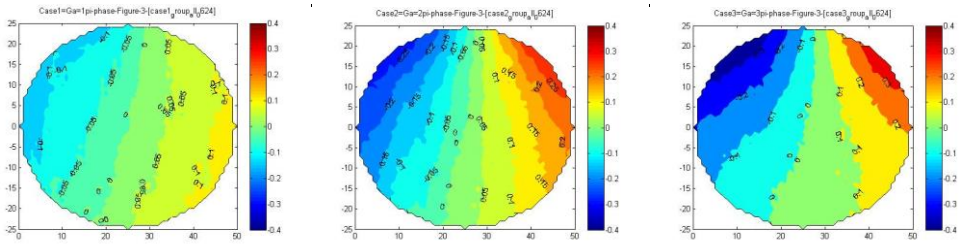

After the Earth field consideration approach 1.

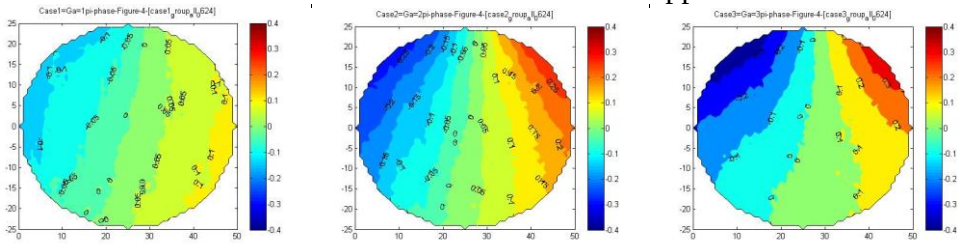

After the Earth field consideration approach 2.

Figure 4.8: Results of the phase information for three cases, before/after the Earth field correction.

3. Additionally, the magnetic field coming from the current feed leads may also affect the phase figure. Therefore, the experiment was repeated with the current leads as far away from the cage coil as possible; however, the obtained phase map shows no significant difference with the first results.

4. Power supply consumption may be another reason. It is the battery groups that supply the amplifiers and act as the negative inputs of the differential amplifier design. Thus, as the experiment runs, the output voltage would decrease slowly and the pin2#2 voltage would change. Therefore the corresponding phase information will be affected, according to the Equations (3.8) and (3.9).

Further work for this study is recommended to increase the efficiency and accuracy of the measurement devices, such as the probe-head design, the amplifier selection and the data acquisition software coding (etc.). As regards the imperfection, the approachable work in the future to improve the device is the calibration of the probe initial position. The initial position of the field mapper probe is the most critical part of the operation of the measurement. If either the probe or the field mapper is not positioned correctly, there may produce the angle problems for the Hall Effect sensor. As described earlier, the Hall Effect sensor output voltage changes as a function of the angle between the Hall plate and the magnetic field vector, which called Hall angle. Therefore, in case of the misalignment of the initial position, the researcher could tape a laser pen at the other end of the aluminum rod, whose excitation point of the laser locates at the center of circle in the longitudinal section. Since the rod is hollow, the technician could turn on the laser pen every time when the measurement starts. Meanwhile, a white paper can be glued onto the birdcage coil setup. Then a more accurate corresponding probe-center position on the birdcage coil can be achieved so as to adjust the probe bar.

CHAPTER 5

SUMMARY AND CONCLUSIONS

5.1 Conclusion

The main purpose of this thesis was to investigate the spatial phase distribution of the magnetic field produced by a DC version of an 8-leg RF encoding birdcage-style coil design.

In this study, a measurement of the static magnetic field was performed. A custom magnetic field vector measurement system based on Hall Effect sensors with signal conditioning and amplification was designed and constructed. The electronic components of the system were selected based on design considerations, tested individually and assembled. Calibration tests showed that the final assembled magnetic field measurement system performed well and had sufficient sensitivity and linearity for this work.

An 8-leg DC-driven birdcage-coil assembly was constructed for this work. Three distinct sets of coil leg currents corresponding to three different phase gradients were tried. Using the custom-built magnetic field measurement system, the B_1 field vector produced by the DC-driven birdcage-coil current was mapped for each case.

The measurements showed that the spatial phase of the magnetic field varied approximately linearly along the assigned axis, which demonstrated that a method of using spatial phase to encode the B_1 field (RF encoding method) is workable.

When the experimentally measured spatial phase was compared to the theoretically simulated spatial phase variation, the main observed difference was a rotation of the experimental profile relative to the expected theoretical profile. Many factors might contribute to

the existence of this rotation. The most likely candidate is a misalignment of the probe axes with the birdcage assembly axes. Another candidate was the influence of the Earth's magnetic field; however, it was found to be minor.

LIST OF REFERENCES

[1] C. Westbrook, *Handbook of MRI Technique*, 3rd ed. Wiley-Blackwell, 2013.

[2] M. A. ;Richar. C. S. Brown, *MRI : basic principles and applications*. Wiley-Liss, 1995.

[3] J. Bellec, C.-Y. Liu, S. B. King, and C. P. Bidinosti, "A Target Field Approach to the Design of RF Phase-Gradient Coils," *Proc. Intl.Soc.Mag.Reson.Med*, vol. 161, no. 19, p. 723, 2011.

[4] J. M. Reddy and V. Prasad, *Step by Step MRI*, 1st ed. CRC Press, 2005.

[5] Z. Popovic and B. D. Popovic, *Introductory Electromagnetics*. Prentice Hall, 1999.

[6] J. W. Pettegrew, *NMR: Principles and Applications to Biomedical Research*. Springer, 1989.

[7] D. C. W. J. N. Wilson, *Mathematical methods in medical imaging II : 15-16 July 1993, San Diego, California*. Society of Photo Optical, 1993.

[8] R. S. MacKay, *Medical Images and Displays: Comparisons of Nuclear Magnetic Resonance, Ultrasound, X-Rays and Other Modalities*, 1st ed. Wiley-Interscience, 1984.

[9] M. T. V. J. A. den Boer, *Magnetic resonance imaging : theory and practice*, 3rd ed. Springer, 2002.

[10] S. Webb, *The Physics of Medical Imaging*, 1st ed. CRC Press, 1988.

[11] *Proceedings, IEEE Workshop on Mathematical Methods in Biomedical Image Analysis : Hilton Head Island, South Carolina, June 11-12, 2000*. IEEE Computer Society, 2000.

[12] J. C. Sharp and S. B. King, "MRI Using Radiofrequency Magnetic Field Phase Gradients," *Magn. Reson. Med.*, vol. 161, no. June 2009, pp. 151–161, 2010.

[13] S. King and J. Sharp, "Method for Radio-frequency nuclear magnetic reasonance imaging," WO 2008/134892 A1, 2008.

[14] C. J. L. Ray Hashman Hashemi, William G. Bradley Jr., *MRI: The Basics*, Third edit. LWW, 2010.

[15] P. Mansfield, P. M. Glover, and J. Beaumont, "Sound generation in gradient coil structures for MRI," *Magn. Reson. Med.*, vol. 39, no. 4, pp. 539–550, 1998.

[16] D. I. Hoult, "Rotating frame zeugmatography.," *Philos. Trans. R. Soc. Lond. B. Biol. Sci.*, vol. 289, pp. 543–547, 1980.

[17] F. Casanova, H. Robert, J. Perlo, and D. Pusiol, "Echo-planar rotating-frame imaging," *J. Magn. Reson.*, vol. 162, pp. 396–401, 2003.

[18] P. C. LAUTERBUR, "Image Formation by Induced Local Interactions: Examples Employing Nuclear Magnetic Resonance," *Nature*, vol. 242. pp. 190–191, 1973.

[19] T. Geva, "Magnetic resonance imaging: historical perspective.," *J. Cardiovasc. Magn. Reson.*, vol. 8, pp. 573–580, 2006.

[20] Segen's Medical Dictionary, "blind study - definition of blind study in the Medical

dictionary - by the Free Online Medical Dictionary, Thesaurus and Encyclopedia.," *Farlex, Inc.*, 2012. [Online]. Available: http://medical-dictionary.thefreedictionary.com/Blind+Study.

[21] Q. Deng, S. B. King, V. Volotovskyy, B. Tomanek, and J. C. Sharp, "B1 transmit phase gradient coil for single-axis TRASE RF encoding.," *Magn. Reson. Imaging*, vol. 31, no. 6, pp. 891–9, Jul. 2013.

[22] J. Jin, *Electromagnetic Analysis and Design in Magnetic Resonance Imaging*, 1st ed. CRC Press, 1998.

[23] T. Neuberger and A. Webb, "Radiofrequency coils for magnetic resonance microscopy," *NMR Biomed.*, vol. 22, no. 9, pp. 975–981, 2009.

[24] O. Ocali and E. Atalar, "Intravascular magnetic resonance imaging using a loopless catheter antenna," *Magn. Reson. Med.*, vol. 37, no. 1, pp. 112–118, 1997.

[25] L. Renaud, M. Armenean, L. Berry, P. Kleimann, P. Morin, M. Pitaval, J. O'Brien, M. Brunet, and H. Saint-Jalmes, "Implantable planar rf microcoils for NMR microspectroscopy," *Sensors Actuators, A Phys.*, vol. 99, no. 3, pp. 244–248, 2002.

[26] A. J. Martin, D. B. Plewes, and R. M. Henkelman, "MR imaging of blood vessels with an intravascular coil," *J Magn Reson Imaging*, vol. 2, no. 4, pp. 421–429, 1992.

[27] L. Axel and C. Hayes, "Surface coil magnetic resonance imaging," *Journal of Computer Assisted Tomography*, vol. 93, no. 5. pp. 11–18, 1985.

[28] J. T. Vaughan, G. Adriany, C. J. Snyder, J. Tian, T. Thiel, L. Bolinger, H. Liu, L. DelaBarre, and K. Ugurbil, "Efficient high-frequency body coil for high-field MRI," *Magn. Reson. Med.*, vol. 52, no. 4, pp. 851–859, 2004.

[29] D. M. G. D.W. Alderman, "An efficient decoupler coil design which reducesheating in conductive samples in superconducting spectrometers.," *J. Magn. Reson*, vol. 36, pp. 447–451, 1979.

[30] K. W. Fishbein, J. C. Mcgowan, and R. G. Spencer, "Hardware for Magnetic Resonance Imaging," *Filippi M, Stefano N, Dousset V, McGowan JC(eds) MR imaging white matter Dis. brain spinal cord.*, pp. 13–28, 2005.

[31] J. C. M. K. Sartor, Massimo Filippi, Nicola de Stefano, Vincent Dousset, *MR Imaging in White Matter Diseases of the Brain and Spinal Cord*, 2005th ed. Springer, 2005.

[32] H. Fujita, G. D. DeMeester, and W. O. Braum, "Open view quadrature birdcage coil," US6316941 B1, 2001.

[33] G. Sarty, "Radio Frequency Coils for Encoding Variable Resolution Spatial Information in Nuclear Magnetic Resonance Signals," 2016.

[34] M. P. Coleman, *An Introduction to Partial Differential Equations with MATLAB*. Chapman and Hall/CRC, 2013.

[35] D. W. T. E. C. Zachmanoglou, *Introduction to Partial Differential Equations with Applications*, 1st ed. Dover Publications, 1987.

[36] P. Monk, *Finite Element Methods for Maxwell's Equations*. Clarendon Press, 2003.

[37] J. R. Claycomb, *Applied Electromagnetics Using Quickfield and Matlab*. Infinity Science Press, 2008.

[38] S. S. Karl Lonngren, *Fundamentals of Electromagnetics with MATLAB*. Scitech Pub Inc, 2005.

[39] C. Vittoria, *Magnetics, Dielectrics, and Wave Propagation with MATLAB® Codes*. CRC Press, 2010.

[40] N. G. H. Pascal Wallisch, Michael E. Lusignan, Marc D. Benayoun, Tanya I. Baker, Adam Seth Dickey, *MATLAB for Neuroscientists: An Introduction to Scientific Computing in MATLAB*, 2nd ed. Academic Press, 2013.

[41] B. Daku, *MATLAB Tutor CD: Learning MATLAB Superfast*. Wiley, 2005.

[42] S. Tumanski, *Handbook of Magnetic Measurements*. CRC Press, 2011.

[43] M. Caruso and T. Bratland, "A new perspective on magnetic field sensing," *Sensors Expo Proc.*, vol. 15, no. 12, pp. 34–47, 1998.

[44] J. E. Lenz, "Review of magnetic sensors," *Proc. IEEE*, vol. 78, no. 6, pp. 973–989, 1990.

[45] E. H. Hall, "On a new Action of the Magnet on Electric Currents," *Am. J. Math.*, vol. 2, pp. 287–292, 1879.

[46] E. H. Hall, "On the New Action of Magnetism on a Permanent Electric Current," The Johns Hopkins University, 1880.

[47] R. S. Popovic, *Hall Effect Devices*. CRC Press, 2003.

[48] Honeywell, "Hall Effect Sensing and Application," 2013.

[49] L. Allegro Microsystem, "A1301/2-Continuous-Time Ratiometric Linear Hall Effect Sensor ICs," 2014.

[50] J. Fraden, *Handbook of Modern Sensors: Physics, Designs, and Applications*, 3rd ed. Springer, 2010.

[51] A. Devices, "AD620 Low Cost, Low Power Instrumentation Amplifier," 2011.

[52] C. Kitchin and L. Counts, "A Designer's Guide to Instrumentation Amplifiers," 2006.

[53] R. E. Simpson, *Introductory Electronics for Scientists and Engineers*, 2nd ed. Addison-Wesley, 1987.

[54] "Positive voltage regulator ICs," 2014.

[55] M. Tallon, G. Scott, and M. Dorma, "Compact MRI Field Mapper-EP495 Capstone Design Project-Engineering Physics, University of Saskatchewan," 2015.

[56] "Shapeoko2 introduction," 2015. [Online]. Available: https://www.inventables.com/technologies/desktop-3d-carving-cnc-mill-kit-shapeoko-2.

[57] "https://github.com/grbl/grbl." [Online]. Available: https://github.com/grbl/grbl.

[58] “Arduino microcontroller module,” 2015. [Online]. Available: http://www.robotshop.com/en/arduino-uno-usb-microcontroller-rev-3.html.

[59] R. T. Merrill, M. W. McElhinny, and P. L. McFadden, *Magnetic Field of the Earth: Paleomagnetism, the Core, and the Deep Mantle*, 1st ed. Academic Press, 2003.

[60] NOAA, “http://www.ngdc.noaa.gov/geomag-web/#igrfwmm,” 2015.